The Astrophysical Journal, 904:146 (26pp), 2020 December 1 https://doi.org/10.3847/1538-4357/abba84

The First Extensive Spectroscopic Study of Young Stars in the North America and Pelican Nebulae

Min Fang[1], Lynne A. Hillenbrand[1], Jinyoung Serena Kim[2], Krzysztof Findeisen[3], Gregory J. Herczeg[4], John M. Carpenter[5], Luisa M. Rebull[6], and Hongchi Wang[7]
[1] Department of Astronomy, California Institute of Technology, Pasadena, CA 91125, USA
[2] Department of Astronomy, University of Arizona, 933 North Cherry Avenue, Tucson, AZ 85721, USA
[3] University of Washington, Department of Astronomy, Seattle, WA 98195, USA
[4] Kavli Institute for Astronomy and Astrophysics, Peking University, Yiheyuan 5, Haidian Qu, 100871 Beijing, People's Republic of China
[5] Joint ALMA Observatory, Alonso de Cordova 3107 Vitacura, Santiago, Chile
[6] Infrared Science Archive (IRSA), IPAC, 1200 East California Boulevard, California Institute of Technology, Pasadena, CA 91125, USA
[7] Purple Mountain Observatory and Key Laboratory of Radio Astronomy, Chinese Academy of Sciences, 2 West Beijing Road, 210008 Nanjing, People's Republic of China
Received 2020 July 16; revised 2020 September 9; accepted 2020 September 10; published 2020 November 27

Abstract

We present a spectroscopic survey of over 3400 potential members in the North America and Pelican Nebulae (NAP) using several low-resolution ($R \approx 1300$–2000) spectrographs: Palomar/Norris, WIYN/Hydra, Keck/DEep Imaging Multi-Object Spectrograph (DEIMOS), and the Multiple Mirror Telescope (MMT)/Hectospec. We identify 580 young stars as likely members of the NAP region based on criteria involving infrared excess, Li I 6708 Å absorption, X-ray emission, parallax, and proper motions. The spectral types of individual spectra are derived by fitting them with templates that are either empirical spectra of pre-main-sequence stars or model atmospheres. The templates are artificially veiled, and a best-fit combination of spectral type and veiling parameter is derived for each star. We use the spectral types with archival photometry to derive *V*-band extinction and stellar luminosity. From the Hertzsprung–Russell diagram, the median age of the young stars is about 1 Myr, with a luminosity dispersion of ∼0.3–0.4 dex. We investigate the photometric variability of the spectroscopic member sample using Zwicky Transient Facility data and conclude that photometric variability, while present, does not significantly contribute to the luminosity dispersion. While larger than the formal errors, the luminosity dispersion is smaller than if veiling were not taken into account in our spectral typing process. The measured ages of the stellar kinematic groups, combined with the inferred ages for embedded stellar populations revealed by Spitzer, suggest a sequential history of star formation in the NAP region.

Unified Astronomy Thesaurus concepts: Stellar accretion disks (1579); Protoplanetary disks (1300); Pre-main sequence stars (1290); Stellar spectral types (2051); Star formation (1569); Star forming regions (1565); Stellar associations (1582)

Supporting material: machine-readable tables

1. Introduction

Galactic O-type stars are rare, with only ∼600 cataloged (Goy 1973; Garmany et al. 1982; Maíz Apellániz et al. 2017). The closest is σ Sco (09.5) at <200 pc. Within about 1 kpc of the Sun there are just a few tens of O-type stars. This small sample includes the famous θ^1 Ori C (O7) and θ^2 Ori A (O9.5) responsible for ionizing the Orion Nebula (O'Dell et al. 2017), as well as several other late O–type stars (such as ι Ori, σ Ori, ζ Ori, the embedded IRS 2b in NGC 2024, and λ Ori) in the Orion molecular cloud complex at ∼400 pc, and S Mon (O7) associated with NGC 2264 at ∼800 pc. Each of these O stars is young enough to still illuminate, and to some extent ionize, the surrounding gas and dust out of which it was recently formed.

The North America and Pelican Nebulae (NAP; NGC 7000 and IC 5070) are parts of an ionized region known as W80 (Matthews & Goss 1980; Reipurth & Schneider 2008). This H II region is ionized mainly[8] by 2MASS J20555125+4352246 (Comerón & Pasquali 2005), also called the Bajamar Star, which has spectral type O3.5–O5 and sits behind the Lynds Dark Nebula LDN 935 (Lynds 1962). The dark region that separates the North America Nebula from the Pelican Nebula is the foreground molecular cloud associated with W80 and has a total mass of about (2–5) × $10^4\,M_\odot$ (Bally & Scoville 1980; Zhang et al. 2014; Kuhn et al. 2020). A distance of 795 pc based on Gaia Data Release 2 (DR2) astrometry (Gaia Collaboration et al. 2016, 2018) is calculated by Kuhn et al. (2020), placing the region somewhat further away than previous estimates (see Reipurth & Schneider 2008 for a review).

Numerous surveys have targeted the young stellar population associated with the region encompassing the NAP and LDN 935. Beginning in the 1950s (see, e.g., Morgan et al. 1955; Herbig 1958; Welin 1973), early studies revealed associations of emission line T Tauri stars near the nebulae.

A significant contribution in understanding star formation in LDN 935 comes from the imaging surveys with the Spitzer Space Telescope (Guieu et al. 2009; Rebull et al. 2011). The Spitzer imaging surveys have discovered more than 2000 young stellar object (YSO) candidates with infrared excess emission and demonstrated the existence of more densely clustered as well as more loosely distributed YSOs (Guieu et al. 2009; Rebull et al. 2011). A majority of the sources with infrared excess are within the boundaries of LDN 935, as opposed to being in the nebular regions, evidencing an active star formation process in this region. The more area-limited

[8] There is a second ionizing source, the O6-type star HD 199579, which is offset from the center of the H II region and moving further toward the periphery; see Kuhn et al. (2020) for a further discussion.

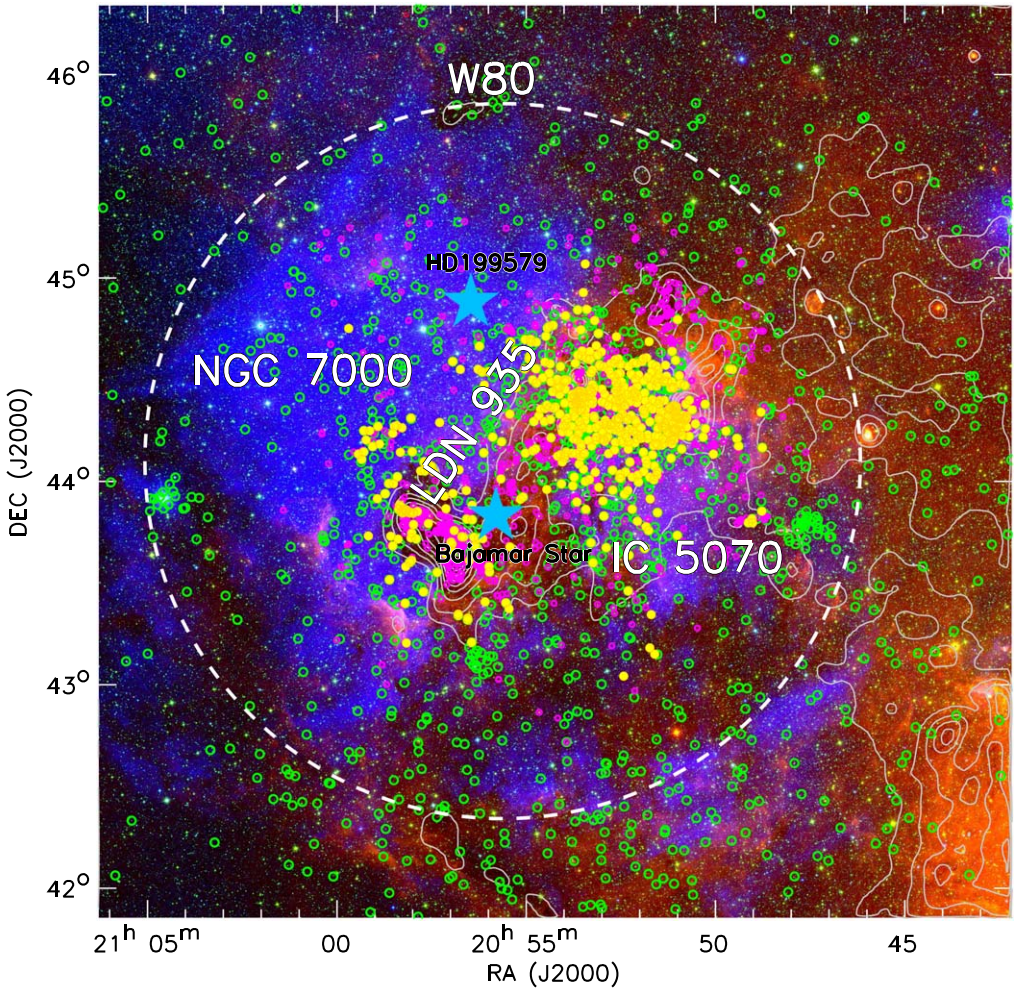

Figure 1. Three-color image of North America Nebula created with the DSS1 *R* band (blue), WISE W1 band (green), and WISE W3 band (red). The gray contours are the Planck 857 μm dust emission. The white dashed circle indicates the approximate boundary of the H II region (Wendker et al. 1983). All the YSO candidates in the field are shown as open circles, magenta for those with infrared excess (Rebull et al. 2011) and green for those identified with Gaia (Kuhn et al. 2020). Our spectroscopically confirmed YSOs are shown as yellow filled circles. The blue filled star symbols mark the H II region's main ionizing source, the Bajamar Star, identified by Comerón & Pasquali (2005), and another member O star HD 199579 in the NAP.

X-ray survey of LDN 935 with the XMM-Newton and Chandra space telescopes by Damiani et al. (2017) confirmed the youth properties of many of the YSO candidates identified with Spitzer, and further revealed hundreds of new YSO candidates without infrared excesses. Figure 1 shows the distribution of YSO candidates in this region. Many of these YSO candidates have been monitored photometrically and show light-curve variations characteristic of YSOs (Findeisen et al. 2013; Bhardwaj et al. 2019).

The NAP region stands in contrast to other nearby star-forming regions having large, well-studied stellar populations, including those associated with the O stars in the Orion complex and the NGC 2264 cluster. Here, only about 60 of the YSO candidates have been studied with spectroscopy. The collection of spectral types is reported in Rebull et al. (2011) and references therein. In this work, we provide the first extensive—though not yet comprehensive—spectroscopic study of YSOs in the NAP.

2. New Observations

We obtained low-resolution ($R \approx 1300$–2000) optical spectra of more than 3400 prospective members of the NAP region over the time period 1998 to 2017. Selection criteria varied over the years and included red optical colors, photometric Hα–R excess, infrared excess, optical photometric variability, and X-ray emission. In assembling targets we were guided by a legacy KPNO/0.9 m CCD survey in BVI, Hα, and R that is partially described in Rebull et al. (2011), the IRAC photometry presented in Guieu et al. (2009), the MIPS photometry presented in Rebull et al. (2011), and the Hα and X-ray data presented in Damiani et al. (2017).

A variety of multi-object spectrographs were used, with the observations cataloged in Table 1 and the instruments, data acquisition, and data reduction described in the subsections below.

2.1. Palomar/Norris Spectra

We used the now-decommissioned Norris multi-object spectrograph (Hamilton et al. 1993) on the 5 m Palomar telescope to obtain spectra of 1294 sources. Norris was a fiber-fed spectrograph with 150 working fibers, each having a 1.″5 aperture. The 20′ field of view was mapped onto a 2048 × 2048 CCD.

Table 1
Log of Spectroscopic Observations

Identifier	Observation (UT Date)	R.A. (J2000)	Decl. (J2000)	Exposure (minutes)	Telescope and Instrument	Selection Criteria[a]	PI
ConFigure 1	2012-05-18	20:52:50	+44:19:32	45	MMT/Hectospec	IRE	Fang
ConFigure 2	2012-05-18	20:52:50	+44:19:32	45	MMT/Hectospec	IRE	Fang
ConFigure 3	2012-06-14	20:54:31	+44:34:32	45	MMT/Hectospec	IRE	Fang
ConFigure 4	2012-06-15	20:57:36	43:58:05	45	MMT/Hectospec	IRE	Fang
ConFigure 5 /MMT1	2012-11-04	20:49:23	+44:39:16	90	MMT/Hectospec	Var, IRE	Hillenbrand
ConFigure 6 /MMT2	2012-12-04	20:56:47	+43:46:02	90	MMT/Hectospec	Var, IRE	Hillenbrand
ConFigure 7 /MMT3	2012-12-06	20:49:48	+43:30:23	90	MMT/Hectospec	Var, IRE	Hillenbrand
ConFigure 8	2017-06-02	20:50:51	+44:08:19	45	MMT/Hectospec	IRE, Var, X-ray	Fang
ConFigure 9	2017-06-02	20:52:53	+44:18:02	45	MMT/Hectospec	IRE, Var, X-ray	Fang
ConFigure 10	2017-06-04	20:53:03	+44:51:03	35	MMT/Hectospec	IRE, Var, X-ray	Fang
ConFigure 11	2017-06-05	20:58:04	+44:33:14	45	MMT/Hectospec	IRE, Var, X-ray	Fang
ConFigure 12	2017-06-05	20:55:35	+44:26:24	45	MMT/Hectospec	IRE, Var, X-ray	Fang
ConFigure 13	2017-06-06	20:59:09	+43:30:45	45	MMT/Hectospec	IRE, Var, X-ray	Fang
ConFigure 14	2017-06-06	20:52:17	+43:26:41	45	MMT/Hectospec	IRE, Var, X-ray	Fang
NANeb H0188 1	1998-06-02	20:51:47	+44:09:00	92	WIYN/Hydra	Hα-R, red BVI	Hillenbrand
NANeb H0188 7	1998-06-05	20:55:08	+44:15:00	90	WIYN/Hydra	Hα-R, red BVI	Hillenbrand
NANeb H0188 9	1998-07-15	20:51:36	+44:10:00	90	WIYN/Hydra	Hα-R, red BVI	Hillenbrand
NANeb H0188 15	1998-07-16	20:57:22	+44:05:45	90	WIYN/Hydra	Hα-R, red BVI	Hillenbrand
NANeb H0188 17	1998-07-16	20:57:18	+44:08:00	90	WIYN/Hydra	Hα-R, red BVI	Hillenbrand
NANeb H0188 23	1998-07-17	20:54:12.5	+44:12:15	90	WIYN/Hydra	Hα-R, red BVI	Hillenbrand
NANeb H0188 25	1998-07-21	20:55:00	+43:30:45	90	WIYN/Hydra	Hα-R, red BVI	Hillenbrand
PTFNAN F6+F8	2012-07-18	20:51:38	+44:30:51	30	Keck/DEIMOS	Var, IRE	Hillenbrand
PTFNAN F7+F9	2012-07-18	20:53:08	+44:18:42	46.7	Keck/DEIMOS	Var, IRE	Hillenbrand
PTFNAN F3+F11	2012-07-18	20:53:07	+44:14:16	30	Keck/DEIMOS	Var, IRE	Hillenbrand
PTFNAN F12	2012-07-17	20:51:36	+44:13:48	45	Keck/DEIMOS	Var, IRE	Hillenbrand
PTFNAN F13+F14	2012-07-17	20:54:13	+44:23:46	40	Keck/DEIMOS	Var, IRE	Hillenbrand
PTFNAN F16+F17	2013-07-10	20:54:47	+44:44:38	45	Keck/DEIMOS	Var, IRE	Hillenbrand
PTFNAN F18+F20	2013-07-10	20:57:29	+44:07:37	45	Keck/DEIMOS	Var, IRE	Hillenbrand
PTFNAN F22+F23+F24	2012-07-18	20:56:37	+43:15:52	30	Keck/DEIMOS	Var, IRE	Hillenbrand
PTFNAN F29	2013-07-10	20:53:59	+43:58:13	45	Keck/DEIMOS	Var, IRE	Hillenbrand
PTFNAN F31	2013-07-10	20:53:13	+43:41:44	45	Keck/DEIMOS	Var, IRE	Hillenbrand
PTFNAN F33+F34	2012-07-18	20:53:26	+44:05:59	30	Keck/DEIMOS	Var, IRE	Hillenbrand
PTFNAN F35	2013-07-10	20:58:12	+43:59:01	40	Keck/DEIMOS	Var, IRE	Hillenbrand
NANeb Brt F1	1999-07-23	20:55:27.8	+44:38:58	12	Palomar/Norris	Hα-R, red BVI	Hillenbrand
NANeb F1	1998-08-14	20 57:15.4	+44:01:23	90	Palomar/Norris	Hα-R, red BVI	Hillenbrand
NANeb F2	1998-08-15	20:57:25.7	+43:32:26	90	Palomar/Norris	Hα-R, red BVI	Hillenbrand
NANeb F3	1998-08-15	20:57:22.7	+43:11:13	90	Palomar/Norris	Hα-R, red BVI	Hillenbrand
NANeb F5	1999-07-21	20:49:52.4	+44:31:25	90	Palomar/Norris	Hα-R, red BVI	Hillenbrand
NANeb F6	1999-07-21	20:50:33.3	+44:19:44	90	Palomar/Norris	Hα-R, red BVI	Hillenbrand
NANeb F7	1999-07-22	20:57:35.8	+43:49:00	90	Palomar/Norris	Hα-R, red BVI	Hillenbrand
NANeb F8	1998-07-23	20:55:32.7	+43:44:32	90	Palomar/Norris	Hα-R, red BVI	Hillenbrand
NANeb F9	1998-07-23	20 55:45.8	+43:26:08	90	Palomar/Norris	Hα-R, red BVI	Hillenbrand
NANeb F10	1999-09-04	20:53:54.0	+43:32:20	120	Palomar/Norris	Hα-R, red BVI	Hillenbrand
NANeb F11	1999-09-05	20:53:44.9	+43:48:18	120	Palomar/Norris	Hα-R, red BVI	Hillenbrand
NANeb F12	1999-09-05	20:53:43.2	+44:07:34	120	Palomar/Norris	Hα-R, red BVI	Hillenbrand
NANeb F13	1999-09-03	20:52:52.8	+44:40:58	120	Palomar/Norris	Hα-R, red BVI	Hillenbrand
NANeb F14	1999-09-04	20:51:30.4	+44:37:41	60	Palomar/Norris	Hα-R, red BVI	Hillenbrand
NANeb F15	1999-09-03	20:52:06.1	+44:17:16	160	Palomar/Norris	Hα-R, red BVI	Hillenbrand
NANeb F17	1999-09-02	20:49:42.6	+44:05:48	120	Palomar/Norris	Hα-R, red BVI	Hillenbrand
NANeb F18	1999-09-02	20:55:26.6	+44:01:03	60	Palomar/Norris	Hα-R, red BVI	Hillenbrand

Note.
[a] IRE: showing infrared excess, Var: showing photometric variability, X-ray: having an X-ray counterpart, Hα-R: showing Hα emission as indicated by the Hα-R color, red BVI: having late spectral type indicated by B-V and V-I colors.

Data were taken in a total of 17 different fiber configurations by observers L. Hillenbrand, T. Small, and J. Carpenter. A 600 line mm^{-1} grating blazed at 5000 Å was used to achieve $R \approx 2000$. On the first observing date the spectra covered 5120–7750 Å, while the remainder of the observations covered 6100–8750 Å.

In each configuration, between 30 and 126 fibers were assigned to a stellar position and between 5 and 59 fibers were

assigned to sky positions. In addition, the set of observations for each configuration included several (typically three) long exposures on target and (typically one to two) interspersed sky exposures offset by ±6″–10″ from the on-target positions. The sky exposure permitted correction on an individual star basis for nebulosity, which is spatially variable. Calibration was achieved using dome flats and internal spectral reference lamps.

Because no filter was used during the Norris observations, some second-order light of bright blue stars in the field was scattered into other fibers, contaminating several spectra longward of 8100 Å.

2.2. WIYN/Hydra Spectra

We used the Hydra multi-object spectrograph (Barden & Armandroff 1995) on the 3.5 m KPNO/WIYN telescope to obtain 645 spectra. Hydra consists of a 1024 × 2048 CCD fed with 99 fibers, each with a 2″ aperture. The 316@7 setting of the bench spectrograph with a GG-495 filter resulted in spectra of 5000 to 10000 Å at $R \sim 1500$.

A total of seven fiber configurations were acquired by KPNO queue observers D. Harmer and D. Wilmarth. The observing strategy was similar to that for the Norris observations, with several on-target exposures and a shorter offset sky exposure.

2.3. Keck/DEIMOS Spectra

A total of 258 spectra were obtained using the multi-slit mode of the Keck/DEep Imaging Multi-Object Spectrograph (DEIMOS; Faber et al. 2003) spectrograph, in 21 different slit mask configurations. A 600 line mm^{-1} grating delivered $R \approx 1350$ spectra covering 5000–9000 Å. The observers were K. Findeisen and L. Hillenbrand.

2.4. MMT/Hectospec Spectra

With the Multiple Mirror Telescope (MMT) and its Hectospec (Fabricant et al. 2005) fiber spectrograph, we obtained spectra in 14 different fiber configurations. There were three separate programs running, with 517 (principal investigator: Fang), 524 (PI: Hillenbrand), and 705 (PI: Fang) stars observed and significantly overlapping selection criteria of candidate members. The observer was often M. Caulkins.

A 270 line mm^{-1} grating was used, resulting in spectra covering 3700–9150 Å at $R \approx 1300$. As with the observations taken using the other fiber instruments, for the MMT sequences three on-source exposures were taken along with one offset sky exposure.

3. Spectroscopic Data Reduction

The Norris and Hydra observations were reduced by G. Herczeg using custom routines written in *IDL*. The bias in each image was corrected for use of the overscan region on the CCD. We determined the trace of each fiber on the detector using the dome flat. The absolute position of each fiber on the detector was determined independently for each individual exposure. We corrected for cosmic rays by identifying deviations from the illumination profile across each fiber on the detector. We corrected for scattered light in the detector by fitting a spline to pixels between fiber positions. We then resampled the counts in each fiber onto a subpixel scale across the dispersion axis to ensure that the extraction window remained constant for each separate on-target, sky, and flat exposure within a given configuration. We measured and subtracted background counts for each fiber based on the counts between fiber positions. We then extracted the spectrum in each fiber using 5 pixel windows in the Hydra spectra and 6 pixels in the Norris spectra. The observations from 1998 August were poorly focused and required 10 pixel extraction windows. The second-order wavelength solution (a FeAr lamp for the Norris observations and a CuAr lamp for the Hydra observations) and the flat-field correction were calculated independently for each fiber.

We obtained a spectrum for a fiber by summing the counts extracted for that fiber from each on-target integration. We corrected for sky and nebular emission by subtracting counts extracted for the same fiber in the sky exposure, scaled to the difference in observing times. In several configurations the sky emission was scaled by an additional 10%–20% to account for changes in the sky transmission. We calculated a master sky spectrum for each configuration by combining the spectra obtained from fibers assigned to the sky, accounting for fiber-to-fiber sensitivity differences. We corrected for changes in the sky emission after comparing the master sky spectrum obtained in the on-target integration and that from the sky integrations. In many cases a fiber in our sky integrations randomly landed on a star or on a region with a much different nebular emission than was detected in the on-target integration. For the configurations with two sky integrations, one or a combination of the two sky fibers was used to subtract sky and nebular emission. In some configurations, the master sky spectrum was used for sky subtraction.

The DEIMOS spectra were reduced by K. Findeisen using a modified version of the DEEP2 pipeline (Cooper et al. 2012; Newman et al. 2013). Images were first bias-corrected and flat-fielded using dome flats. After spectral extraction, the one-dimensional spectra were wavelength-calibrated but not flux-calibrated. We then corrected for sky and nebular emission by subtracting a fit to the adjacent off-source spectrum within each slit. The final spectra spanned approximately ≈4400–9500 Å, though the range of any particular star shifted by up to ±500 Å depending on the slit location within the mask. Cosmic rays were left uncorrected by the pipeline and were cleaned by hand from the final spectra.

The Hectospec spectra with PI Hillenbrand were processed by S. Tokarz using the Hecto Pipeline (Mink et al. 2007). Following bias correction, flat-fielding, spectral extraction, and wavelength calibration, the sky exposures were scaled and subtracted from the averaged on-source exposures. The Hectospec spectra with PI Fang were reduced using IRAF routines following the standard procedures, as described in Fang et al. (2013).

4. Assembly of Catalog Photometry and Variability Data

In order to construct the spectral energy distribution (SED) of each source, we used optical photometry in the *g*, *r*, *i*, *z*, and *y* bands from Pan-STARRS (Chambers et al. 2016) and in the *G*, G_{BP}, and G_{RP} bands from Gaia DR2 (Gaia Collaboration et al. 2016, 2018), near-infrared photometry in the *J*, *H*, and K_S bands from the Two Micron All Sky Survey (2MASS; Skrutskie et al. 2006), and near- and mid-infrared photometry in Spitzer [3.6], [4.5], [5.8], [8.0], and [24]. The Spitzer data came from two different sources: for the YSO candidates identified with infrared excess emission we used the photometry of Guieu et al. (2009) and Rebull et al. (2011), while for other sources (mostly foreground/background field stars) we

Table 2
Stars Used in Deriving the Instrumental Response Functions

Name	R.A. (J2000)	Decl. (J2000)	Adopted $T_{\rm eff}$ (K)	Wavelength Ranges (Å)	Instruments
BD-06 1263	05 37 41.45	−06 33 57.8	7000	3700–9150	Hectospec
BSD 40-279	20 52 07.65	+44 03 44.4	18,500	4880–10240	Hydra
Cl* IC 4665 P 150	17 47 33.32	+05 31 46.0	5800	4210–9380	DEIMOS
TYC 3179-1399-1	20 57 36.23	+43 57 27.9	6500	5120–7740	Norris
BSD 40-1004	20 56 10.96	+44 39 13.0	10,500	6120–8760	Norris

used the aperture photometry at 3.″8 from the Spitzer Enhanced Imaging Products[9] (SEIP; Teplitz et al. 2012).

We also inspected the variability of the young stars in the NAP using photometric data from the Zwicky Transient Facility (ZTF), which is a time-domain survey mainly in the g and r bands that started in 2017 at Palomar Observatory (Masci et al. 2019). In this work, we search ZTF DR2 with the data taken between 2018 April and 2019 June for the NAP region. Only r-band photometry is used, as our targets typically are somewhat extincted sources.

5. Data Analysis

5.1. Spectral Classification

Our spectral data are collected from multiple instruments. We derive the instrument response function for each observation set using one early-type star observed with the corresponding instrument and spectrograph setup. A list of the stars used for the individual instruments is given in Table 2. The detailed procedure is as follows.

First, we obtain the BOSZ Kurucz model atmosphere (Mészáros et al. 2012) appropriate for each source. Next, we fit the broadband photometry from Gaia and 2MASS for each source using the aforementioned model with two free parameters: extinction and stellar angular radius, as in Fang et al. (2009) and Fang et al. (2013). Then, we shift and rotationally broaden the best-fit model atmosphere and degrade it to the spectral resolution of the individual instruments. The ratio between the observed and model spectra is fitted with separate polynomial functions for different wavelength ranges. From the fitting, we derive the instrument response function of the individual instruments.

The response function is then employed to correct the observed spectra to the same relative flux scale as a function of wavelength. We stress that this procedure does not achieve truly flux-calibrated spectra but instead removes the instrumental signatures in the spectra. The corrected spectra are then normalized by their flux at 7465 Å.

We perform spectral classification of the normalized spectra by fitting them with two sets of spectral templates: one collected from the Very Large Telescope/X-shooter for pre-main-sequence (PMS) stars with spectral types ranging from G6 to M9.5 (Manara et al. 2013, 2017; Rugel et al. 2018; see also Fang et al. 2020) and the other from a combination of model atmospheres with $T_{\rm eff}$ = 2775–35,000 K, surface gravity $\log g$ = 3.5–5, and $v \sin i$ = 0–150 km s^{-1} with models for $T_{\rm eff}$ = 2775–12,000 K from Husser et al. (2013) and for $T_{\rm eff}$ above 12,000 K from Mészáros et al. (2012). For the X-shooter templates, we interpolate them into two sets for use as described below, one with a grid spacing of 1.0 spectral subclass and the other with a grid spacing of 0.2 spectral subclasses. For the model atmospheres, we interpolate the grid in steps of 25 K for $T_{\rm eff}$ = 2775–7000 K, 50 K for $T_{\rm eff}$ = 7000–12,000 K, 500 K for $T_{\rm eff}$ = 12,000–20,000 K, and 1000 K for $T_{\rm eff}$ = 20,000–35,000 K and in steps of 0.25 for $\log g$. Before fitting to our data, the spectral templates are degraded to the spectral resolution of the observed spectra (typically 1500–2000), which have been corrected by the instrument response function.

To mimic the filling effect on the photospheric absorption lines due to excess emission from the accretion shocks, an excess flux is added to the spectral template, parameterized as $r_{\rm ex,7465} = \frac{F_{\rm excess,7465}}{F_{\rm phot,7465}}$, where r_{7465} is the veiling at 7465 Å, $F_{\rm excess,7465}$ is the excess flux at 7465 Å, and $F_{\rm phot,7465}$ is the underlying photospheric emission at 7465 Å. The shape of the accretion continuum spectrum is approximated as a constant, following, e.g., Herczeg & Hillenbrand (2014). Finally, the veiled spectral templates are reddened, parameterized by A_V and using the extinction law from Cardelli et al. (1989), adopting a total-to-selective extinction value R_V = 3.1 (typical of interstellar medium dust). For comparison to the data, each processed template is then renormalized by the flux at 7465 Å.

These steps are described in further detail below, where we make use of both the empirical spectral templates and the model atmospheres. We perform the fitting of each observed spectrum considering two cases: one without veiling and the other including veiling. For the fitting, we have four free parameters: spectral type (SpT), relative radial velocity (ΔRV) between the template and the target spectrum, r_{7465}, and visual extinction (A_V). We divide our procedure into two steps:

1. *Step 1*. We start the fitting using the templates with the coarse grid (1 subclass). First, we set ΔRV = 0 km s^{-1} and normalize the template spectra by the flux at 7465 Å, add $r_{\rm ex,7465}$ to the normalized templates, and redden the veiled templates with a visual extinction A_V. Then, we divide the reddened templates by the target spectrum and fit the ratio by an order 3 polynomial function so as to correct for the possible difference in shape between the templates and the target spectrum. The polynomial function is then applied to the templates. For individual templates, r_{7465} is fixed to zero for nonveiling fitting and varies from 0 to 5.7 with a grid step of 0.1, and A_V varies from 0 to 10 mag stepped by 0.5 mag. The best-fit template is obtained by minimizing the reduced χ^2 ($\chi^2_{\rm r}$). After finding the best-fit template, we then vary ΔRV from −80 to +80 km s^{-1} with a grid step of 2 km s^{-1} and shift the best-fit template by ΔRV to find the best ΔRV value by minimizing $\chi^2_{\rm r}$. During the fitting, the emission

[9] We noticed that some sources had unreliable SEIP photometry and discuss this in Appendix A. For these sources, we used point-spread function fitting photometry that was newly derived as described in Fang et al. (2009). This mixing of photometry did not affect the results for most members of the NAP whose photometry was collected from Rebull et al. (2011), but it did clean up the SEDs of field main-sequence stars with large scatter using the aperture photometry from SEIP.

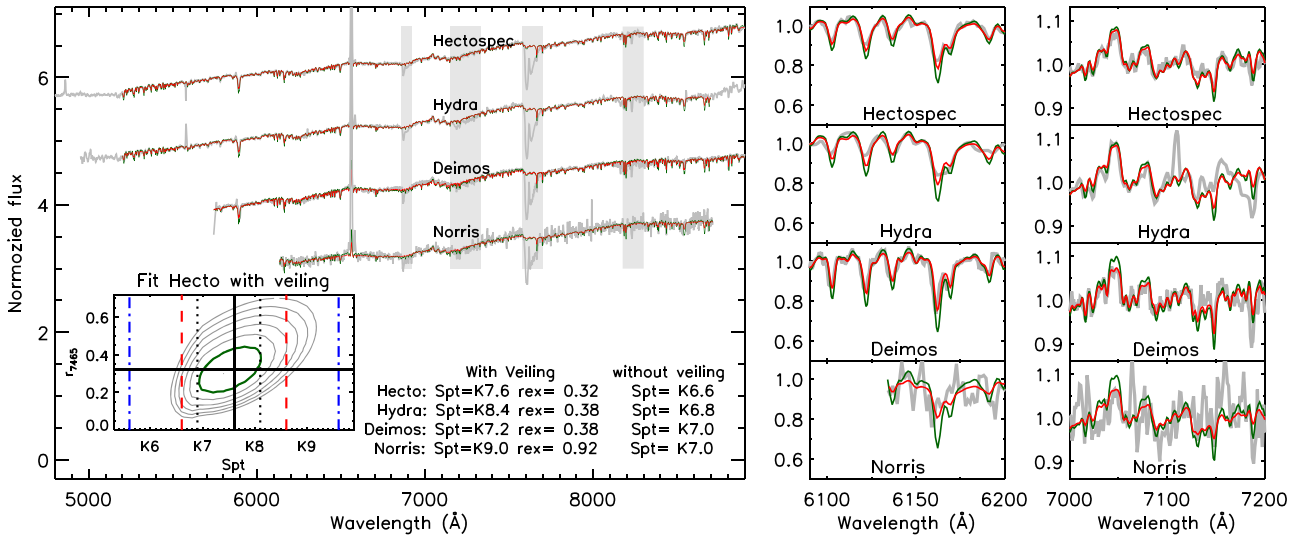

Figure 2. Illustration of our spectral template fitting method for Source ID 103, which was observed with all the four spectrographs used in this study. Left: best-fit X-shooter empirical spectral templates (red including veiling in the template model and green without veiling) overplotted on the observed spectra (gray). Vertically oriented gray bars indicate regions masked due to potential contamination from emission lines or telluric features. The inset contours show the distribution of the reduced χ^2 derived from fitting the Hectospec spectrum with X-shooter templates with different combinations of SpT and r_{7465}. The green contour is for the minimum reduced χ^2+0.05. The solid lines show the $\mathrm{SpT}^{\mathrm{best}}$ (vertical solid line) and r_{7465}^{best} (horizontal solid line) with the minimum reduced χ^2. The two vertical dotted lines show the spectral type range with χ^2_{r} within $\chi^2_{\mathrm{r,min}}$+0.05. Vertical red dashed and blue dashed–dotted lines are used to qualify our spectral classification (see Section 5.1). Right: zoomed-in comparison of the target spectra and the best-fit template with (red) and without (green) veiling within 6090–6200 Å and 7000–7200 Å. The veiled model (red) is a better fit to the observed spectrum (gray).

lines and telluric features are excluded. We then use the best ΔRV as an input and repeat Step 1. Finally, we obtain the best-fit values for the four parameters $\mathrm{SpT}^{\mathrm{best}}$, A_V^{best}, $\Delta\mathrm{RV}^{\mathrm{best}}$, and r_{7465}^{best} in the case of the veiling fitting or three parameters (without r_{7465}^{best}) in the case of the nonveiling fitting.

2. *Step 2*. In this step, the procedure is the same as in Step 1, but we use the template grid with a finer spacing of 0.2 subclasses, and we vary the spectral type from $\mathrm{SpT}^{\mathrm{best}}$–2 to $\mathrm{SpT}^{\mathrm{best}}$+2, A_V from A_V^{best}–2 to A_V^{best}+2 with a grid spacing of 0.2, ΔRV from $\Delta\mathrm{RV}^{\mathrm{best}}$–20 to $\Delta\mathrm{RV}^{\mathrm{best}}$+20 with a grid spacing of 1 km s^{-1}, and r_{7465} from r_{7465}^{best}–0.4 to r_{7465}^{best}+0.4 with a grid spacing of 0.04, along with a value of 0 for the nonveiling fitting. We find the best combination of r_{7465} and SpT when fitting with veiling and the best SpT when fitting without veiling, by minimizing χ^2_{r} (with the minimum χ^2_{r} denoted as $\chi^2_{\mathrm{r,min}}$). The A_V resulting from the fitting is not used given that we have done some normalization during the fitting. A_V is derived instead from the broadband photometry (see Section 5.2).
3. *Step 3*. We now use the model atmospheres in place of the empirical spectral templates, and we repeat Step 1 to refit each target spectrum. In quoting our final results, we use the best-fit model atmospheres only for spectra earlier than type K. This is motivated by the fact that for these earlier spectral types, the empirical templates are not well established, and the available grid is sparse.

Figure 2 shows one example of our spectral fitting for Source ID 103 compared to a spectral model based on the empirical X-shooter templates. This object has been observed with all four instruments. Best-fit templates are illustrated for each observation in both the nonveiling and veiling cases. In order to determine which templates can fit the observations, we check the fits within two spectral ranges: 6090–6200 Å, where there are several metallic lines, e.g., Fe I and Ca I, and 7000–7200 Å, where there are TiO bands. For this source, the fitting with veiling better matches the observations. For three spectra from Hectospec, Hydra, and DEIMOS with large wavelength coverage and good data quality, the spectral types from them agree with each other within one subclass. Figure 3 shows another example of our spectral fitting for Source ID 232. In this case the nonveiling fitting can better fit the observed spectra of the source.

In general, we quantify the spectral classification by comparing the derived spectral type range (SpT1–SpT2) given by χ^2_{r} within $\chi^2_{\mathrm{r,min}}$+0.05, considering thresholds defined based on the spectral types. In our figures, we set two thresholds given by the vertical red dashed lines and vertical blue dashed–dotted lines. For values of $\mathrm{SpT}^{\mathrm{best}}$ earlier than K0, these lines correspond to $\mathrm{SpT}^{\mathrm{best}} \pm 2$ and $\mathrm{SpT}^{\mathrm{best}} \pm 4$, respectively. For values of $\mathrm{SpT}^{\mathrm{best}}$ between K0 and M0, they are $\mathrm{SpT}^{\mathrm{best}} \pm 1$ and $\mathrm{SpT}^{\mathrm{best}} \pm 2$, respectively. And for values of $\mathrm{SpT}^{\mathrm{best}}$ later than M0, they are $\mathrm{SpT}^{\mathrm{best}} \pm 0.5$ and $\mathrm{SpT}^{\mathrm{best}} \pm 1$, respectively. We consider the spectral classification as well determined (Rank 1 in our tables) when the spectral type range SpT1–SpT2 is within the narrower threshold, as fairly determined (Rank 2 in our tables) when SpT1–SpT2 is between the thresholds, and as poorly determined (Rank 3 in our tables) when SpT1–SpT2 is beyond the wider threshold.

In our data set, there are 130 sources with Hectospec spectra observed at two epochs. There are also 90 sources observed with both Hectospec and Hydra, 64 with both Hectospec and DEIMOS, and 47 with both Hectospec and Norris. Figure 4 compares the spectral types derived for the same objects taken with Hectospec at different observational times (left) and with different instruments (right). The spectral types from different spectra for the same sources agree well with each other, especially for those sources with high veiling, demonstrating the robustness of the instrumental response corrections and the spectral normalization procedures described above. While there

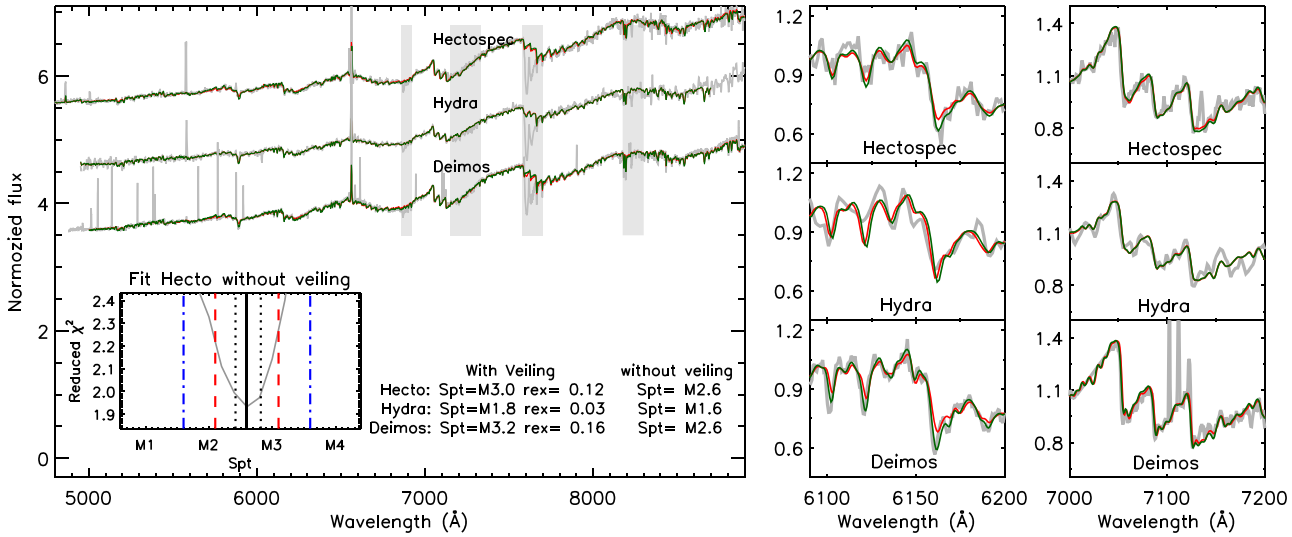

Figure 3. Same as Figure 2, but for Source ID 232. In this case the nonveiled model (green) is the preferred fit to the observed spectrum (gray). In the left panel, the inset shows the distribution of reduced χ^2 derived from fitting the Hectospec spectrum with X-shooter templates having different SpT. Vertical lines represent the same quantities as in Figure 2.

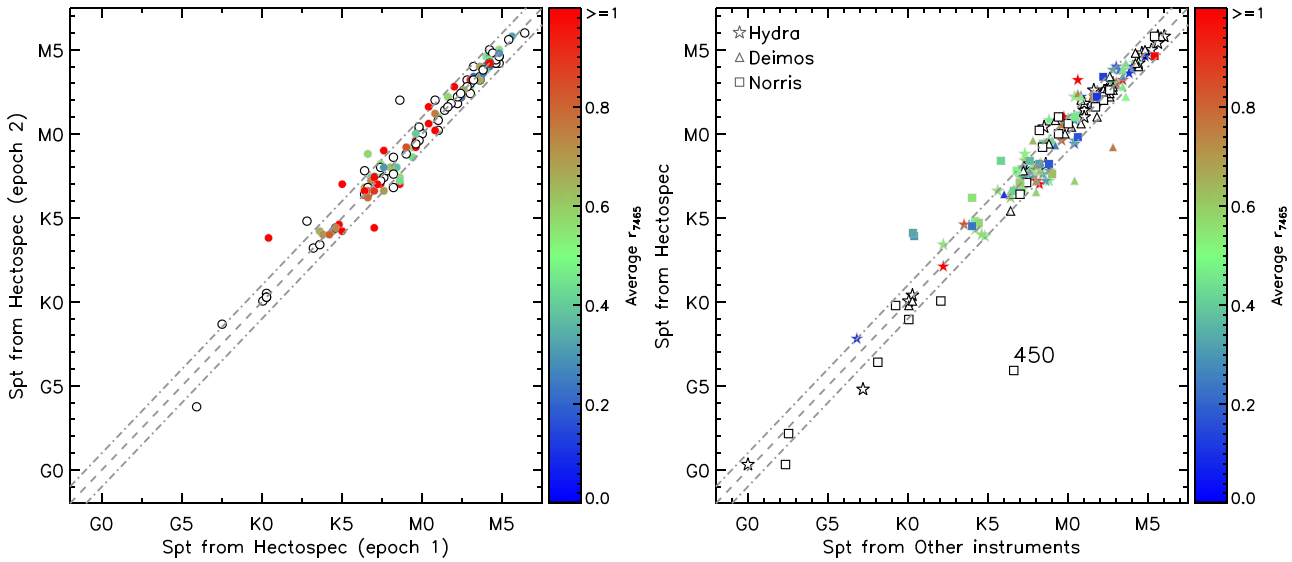

Figure 4. Left: comparison of spectral types derived from the Hectospec spectra for the same stars, observed at different epochs. Right: comparison of spectral types derived from Hectospec with those derived from other instruments for the same stars. In both panels, dashed lines indicate the one-to-one relationship, while dashed–dotted lines are offset by ±2 spectral subclasses from the one-to-one lines. In each panel, the symbols are color-coded according to their average r_{7465} (open symbols represent sources with $r_{7465} = 0$).

are no systematic offsets between these spectral types, the median difference among the Hectospec data is 0.2 subclasses, and that between Hectospec and the other instruments is 0.4–0.6 subclasses. These differences are within the typically quoted spectral typing accuracy of 0.5–1 spectral subclass.

We highlight in the right panel of Figure 4 that there is one source, ID 450, that shows a large variation in the derived spectral types. We find K6.6 from the Norris spectrum and G5.9 from the Hectospec spectrum. This object is the known FU Ori star PTF 10qpf (also named LkHα 188-G4 and HBC 722), which started its outburst around 2010 (Semkov et al. 2010; Miller et al. 2011). The object was observed in its preoutburst stage on 1998 August 14 with Norris and in its post-outburst stage on 2017 June 5. The spectral types are consistent with those in the literature for both the preoutburst (Cohen & Kuhi 1979) and the post-outburst stages (Miller et al. 2011). In this work, we adopt K6.6 as the spectral type, in order to derive the stellar properties of the FU Ori progenitor.

Figure 5 compares the spectral types for the same spectral fitting with and without veiling. As expected, the fitting without consideration of veiling tends to produce an earlier type than the fitting with veiling. The offset depends on the strength of the veiling, with the difference typically 0–1 subclass for $r_{7465} \lesssim 0.2$, 1–2 subclasses for $r_{7465} \sim 0.2$–0.6, and >2 subclasses for $r_{7465} \gtrsim 0.6$. The comparisons emphasize the necessity for considering veiling effects when performing spectral classification for accreting young stars, as already shown in Herczeg & Hillenbrand (2014) and Fang et al. (2020). The results on the spectral classification for the members of the NAP (see Section 5.3) are listed in Table 3. The importance of the veiling correction to the derived luminosity (see Section 5.2 in the following) is illustrated in Figure 6.

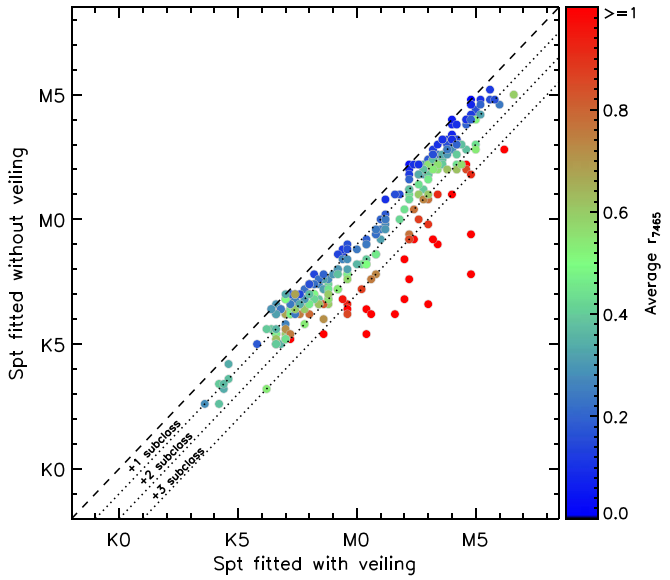

Figure 5. Comparison of spectral types derived for the same stars by fitting without and with accounting for spectral veiling. The dashed line indicates the one-to-one relationship, while the dotted lines are offset by 1, 2, and 3 spectral subclasses from the one-to-one lines. The symbols are color-coded according to their average r_{7465}.

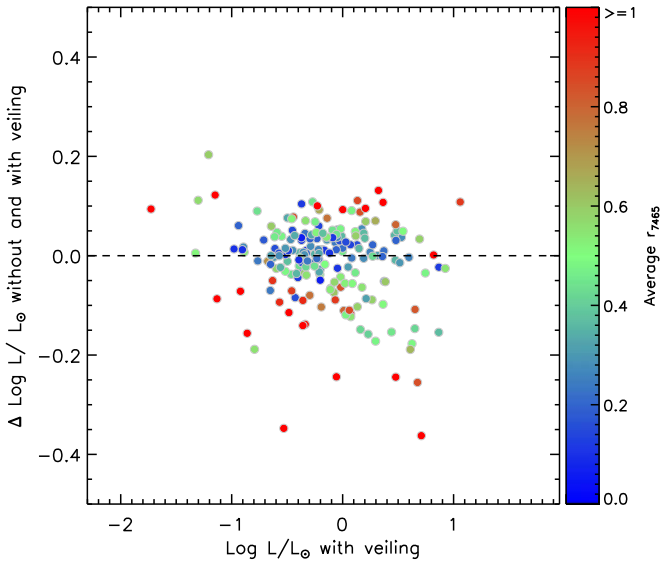

Figure 6. Comparison of luminosities derived for the same stars by fitting without and with accounting for spectral veiling. The symbols are color-coded according to their average r_{7465}.

5.2. Extinction and Stellar Luminosity

Although we have a preliminary A_V estimate from the optical spectrum fitting process described above, the optical spectra are not flux-calibrated very well. We thus improve our confidence in the A_V values by considering the broader SED to fit for both the extinction and the stellar luminosity of each young star in our sample. In general, we use the photometry in g', r', i', and z' from Pan-STARRS, in G, $G_{\rm BP}$, and $G_{\rm RP}$ from Gaia, and in the J band from 2MASS. For our SED fit, we match the optical and near-infrared photometry with a veiled and reddened model atmosphere having the effective temperature derived from our spectral classification and a veiled and reddened X-shooter empirical spectral template having the same spectral type as the source. In most cases there is agreement between the methods, with the details discussed below.

The SED fitting procedure employs three parameters: the source angular diameter θ, the veiling r_{7465}, and the extinction A_V. We first veil the model atmosphere, adopting a value of r_{7465} (either that derived from our spectral fitting above or a free parameter in the SED model). The form of the excess emission flux as a function of wavelength can then be characterized as follows:

$$F_\lambda^{\rm ex} = \begin{cases} F_{7456}^{\rm phot} \times r_{7465} & \text{if } \lambda < 0.9\ \mu\text{m} \\ F_{7456}^{\rm phot} \times r_{7465} \times \dfrac{1.3-\lambda}{1.3\text{–}0.9} & \text{if } 0.9\ \mu\text{m} \leqslant \lambda \leqslant 1.3\ \mu\text{m} \\ 0 & \text{if } \lambda > 1.3\ \mu\text{m} \end{cases} \quad (1)$$

where $F_{7456}^{\rm phot}$ is the photospheric emission at 7465 Å and λ is the wavelength in units of micrometers. According to Fischer et al. (2011), excess emission from accretion (which peaks in the ultraviolet) can still contribute at the J band in some cases. Furthermore, in order to avoid any sharp jump in the flux of our model SED, we allow the excess emission flux from veiling to decrease from a value that we have assumed is flat with wavelength in the optical, to zero over the wavelength range 0.9–1.3 μm. Beyond 1.3 μm we assume there is no veiling.[10]

As above, we use the extinction law of Cardelli et al. (1989) to redden the veiled model atmospheres, adopting $R_V = 3.1$. Synthetic photometry is calculated in the bands of the assembled SEDs by integrating the intensity of the (reddened) model atmospheres over the spectral response curve for each filter and is compared with the observations. The model atmospheres are the same as the ones used for the spectral classification, but considering only $\log g = 4.0$. The high spectral resolution models from Husser et al. (2013) extend to 2.5 μm, and for longer wavelengths we use the BT-Settl model atmospheres (Allard et al. 2011) with solar abundances from Asplund et al. (2009) at the corresponding $T_{\rm eff}$. This combination of models does not affect the SED fitting since our SED fitting goes only to the 2MASS J band. By minimizing χ^2, the optimum values for the three free parameters are achieved. To investigate how veiling can affect the final results, we consider two cases in the fitting: (1) setting r_{7465} to the same value as the one from the spectral fitting described above and (2) setting r_{7465} as a free parameter. Although both cases are improper for any source showing strong brightness variability, and neither case may be proper in other circumstances, the SED fitting method can give us a sense of the uncertainty on the stellar properties when the results are compared to the results on veiling and extinction derived from the spectral fitting process.

As above for the spectral fitting, here for the SED fitting, we use model atmospheres for spectral types G5 and earlier, and we replace the model atmosphere with the X-shooter empirical templates for the majority of the sample with spectral types of G6 to M. In the fitting of the broadband photometry, we have three parameters: $F_{7456}^{\rm phot}$, A_V, and r_{7465}. $F_{7456}^{\rm phot}$ is the photospheric emission at 7465 Å, and the other two parameters are the same as in the earlier fitting processes. In Figure 7, we show an

[10] This could create an artificial jump in the SED for a small number of sources with strong accretion (high r_{7465}).

Table 3
Young Stars in the NAP

							Hectospec				Hydra				DEIMOS				Norris			
							With Veiling				With Veiling				With Veiling				With Veiling			
ID	R.A.			Decl.			SPT	r_{7465}	No Veiling SPT	M[a]	SPT	r_{7465}	No Veiling SPT	M[a]	SPT	r_{7465}	No Veiling SPT	M[a]	SPT	r_{7465}	No Veiling SPT	M[a]
1	20	48	50.71	+43	49	49.7	Cont	High	…	…	…	…	…	…	…	…	…	…	…	…	…	…
2	20	49	11.78	+44	12	32.9	K7.4	0.14	K7.0	1	…	…	…	…	…	…	…	…	…	…	…	…
3	20	49	14.47	+44	14	49.9	M5.0	0.02	M4.8	1	…	…	…	…	…	…	…	…	…	…	…	…
4	20	49	20.30	+44	35	13.5	M2.6	0.04	M2.4	1	…	…	…	…	…	…	…	…	…	…	…	…
5	20	49	24.76	+44	35	21.8	M5.6	0.02	M5.6	1	…	…	…	…	…	…	…	…	…	…	…	…
6	20	49	32.19	+44	17	03.1	M1.2	0.18	M0.2	1	…	…	…	…	…	…	…	…	…	…	…	…
7	20	49	53.51	+44	10	17.3	…	…	…	…	…	…	…	…	…	…	…	…	M3.6	0.02	M3.4	1
8	20	50	06.05	+44	17	49.0	…	…	…	…	M4.2	0.08	M4.0	1	…	…	…	…	…	…	…	…
9	20	50	09.92	+44	15	21.3	M1.4, M1.8	0.02, 0.12	M1.4, M1.4	1	…	…	…	…	…	…	…	…	…	…	…	…
10	20	50	22.43	+44	19	17.6	…	…	…	…	M4.0	0.36	M2.8	1	M4.0	0.02	M4.0	1	…	…	…	…
11	20	50	27.71	+44	23	29.1	K3.8	0.49	G8.4	1	…	…	…	…	…	…	…	…	…	…	…	…

Note.
[a] 1: Using X-Shooter PMS spectral templates; 2: using model atmospheres.

(This table is available in its entirety in machine-readable form.)

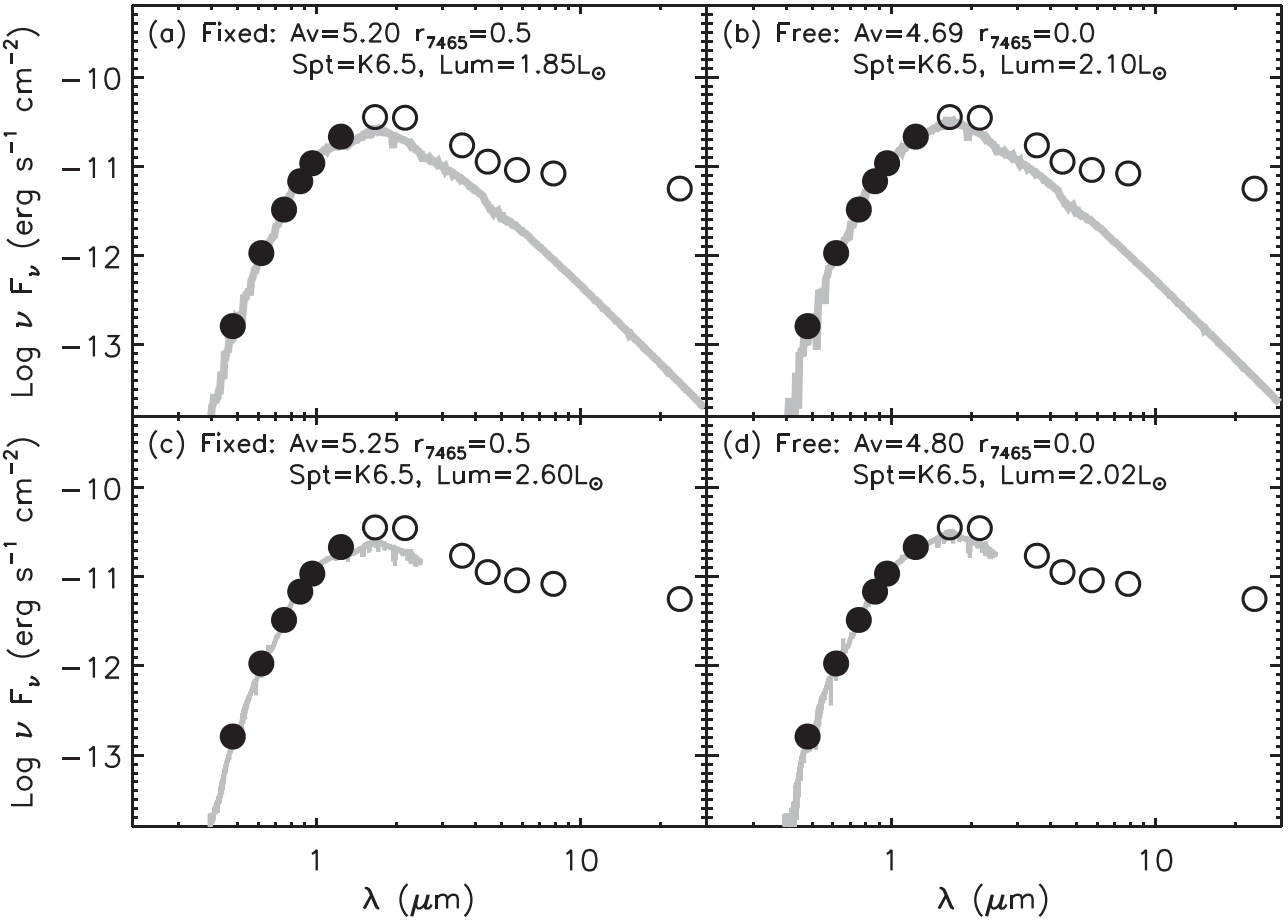

Figure 7. Example of fitting broadband photometry for Source ID 12 using model atmospheres (top panels) and X-shooter empirical templates (bottom panels). Filled circles represent the photometry used for the SED fitting, while open circles are not used to constrain the fits.

example illustrating the best-fit results with the models and with the X-shooter empirical templates.

In Figure 8, taking the confirmed members in the NAP (see Section 5.3), we compare our methods for deriving the extinction values at the V band (upper panel) and the stellar luminosities (bottom panel) through SED fitting using model atmospheres versus X-shooter templates. The earliest type of the sources shown in the figure is G6 due to the limit of the spectral type range of X-shooter templates. For most of the sources, there are no significant shifts between the A_V from the two methods with the mean difference between them being about 0.10 dex. But when there are differences, model fitting tends to give larger A_V. This is especially true at $A_V < 2$. The $L_\star$ comparison between the two methods shows general consistency when $L_\star \gtrsim 0.4\ L_\odot$; however, at lower luminosities there is a systematic shift between the $L_\star$ values of the two methods with the X-shooter template values 0.05 dex lower. This shift may be due to the increasing difference between the stellar models and observed spectra toward the later spectral type.

5.3. Membership Selection

In the previous section we assess the foreground extinction and the basic stellar properties of temperature and luminosity for our sample. In addition, we derive the spectral veiling at red optical wavelengths, which is a proxy for the infall and accretion of material onto the star. The evidence for ongoing accretion is one indicator of stellar youth. Other stellar youth indicators are investigated in this section. These include lithium absorption in the spectra, which would indicate an age younger than the lithium depletion time; X-ray emission, indicative of coronal activity, which is known to decline with age; and infrared excess, indicative of a dusty circumstellar disk that can feed the disk-to-star accretion that is detected as spectral veiling. We investigate each of these measures of stellar youth in the first three subsections below. Then in the fourth subsection we use Gaia astrometry to confirm the membership of the lithium, infrared excess, and X-ray selected samples. All the sources discussed in the section are among our spectroscopic sample.

5.3.1. Li I Absorption

We use the presence of the Li I absorption line at 6708 Å to characterize the youth of the stars. In Figure 9, we show examples of Li I λ6708 detection. For four individual sources, we show both the object spectrum and the spectrum of an older field star with a similar spectral type, for comparison. We visually inspect all spectral targets and detect Li I λ6708 absorption from 350 sources.

5.3.2. X-Rays

Parts of the have been observed and studied with the X-ray space telescopes XMM-Newton and Chandra (Damiani et al. 2017). We match our targets with the X-ray sources using the

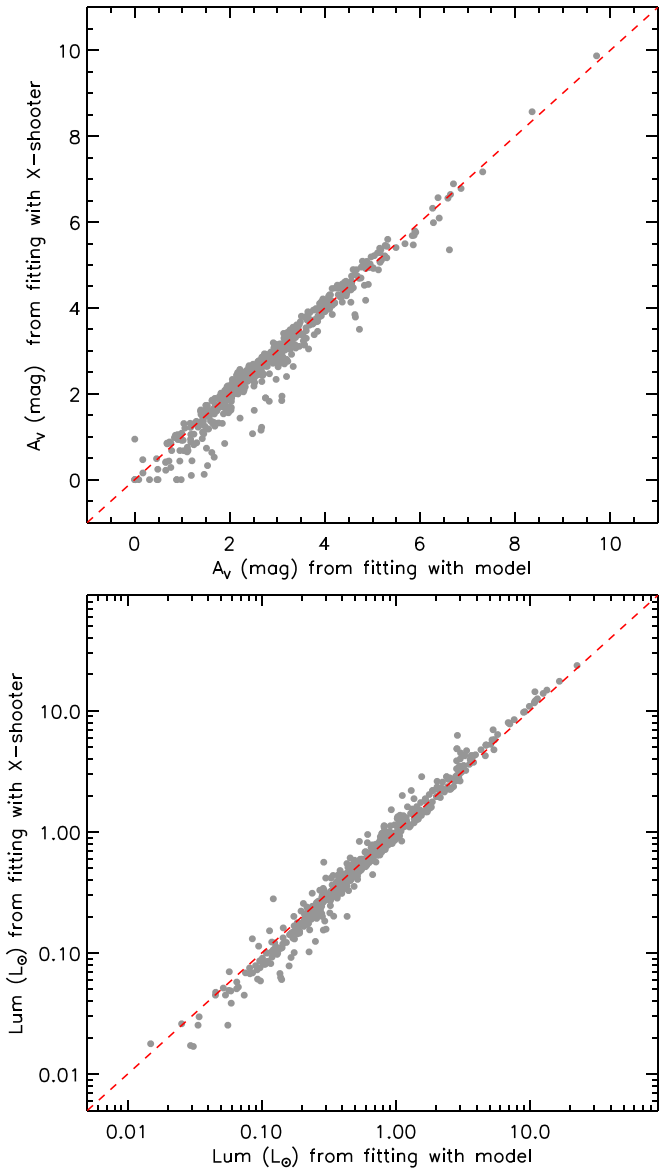

Figure 8. Comparison of extinction in V band (top) and stellar luminosity (bottom) from spectral fitting using model atmosphere and X-shooter templates. In each panel, the red dashed line indicates a 1:1 relation.

positional uncertainties of the X-ray sources as the tolerances. In this way, we find 175 counterparts for the X-ray sources in Damiani et al. (2017) in our spectroscopic sample.

5.3.3. Infrared Excess

For each source with an optical spectrum in our sample, we determine whether there is evidence for infrared excess emission by comparing the appropriate BT-Settl model atmosphere with two versions of the infrared spectral slope, $\alpha_{3.6-8}$ and $\alpha_{3.6-24}$, calculated with the Spitzer photometric data and corresponding to the spectral range of [3.6] to [8.0] and [3.6] to [24], respectively, as done in Fang et al. (2017).

Figure 10 shows the two infrared spectral slopes versus the spectral types for our sources. In the figure, the spectral slopes of the reference BT-Settl atmospheric models (Allard et al. 2011) are calculated allowing for a 10% uncertainty in the

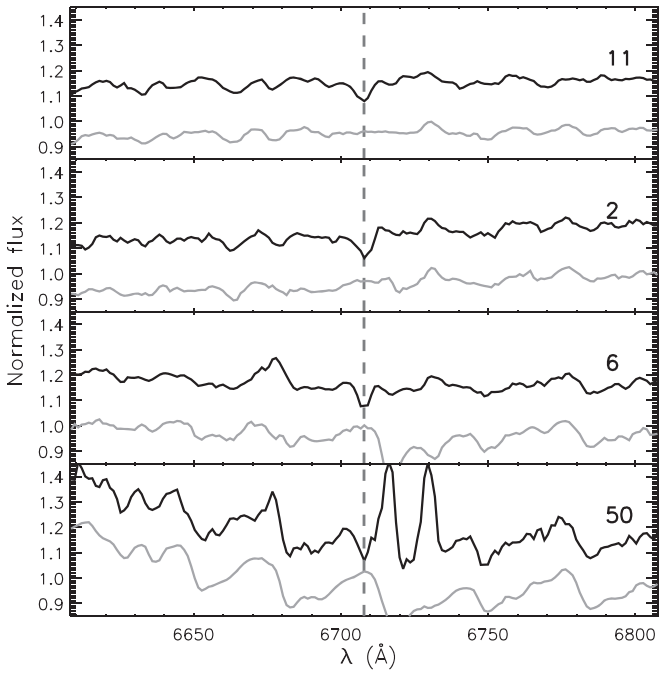

Figure 9. Examples of Li I λ6708 detection for four of our targets, IDs 11, 2, 6, and 50, ordered by their spectral types ~K4 to M3 from top to bottom. In each panel, there are two spectra: one for a young star (black) and the other for a field star (gray) of similar spectral type. For comparison purposes, the spectra are normalized and shifted.

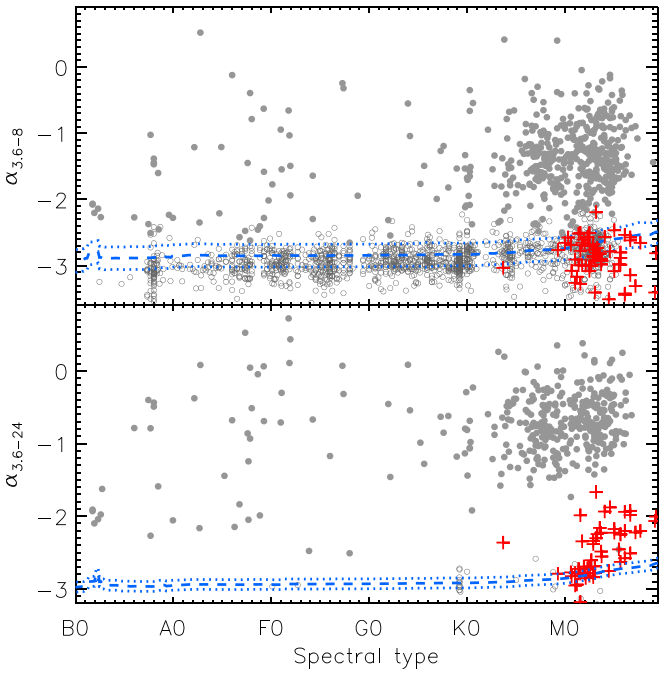

Figure 10. Dereddened Spitzer infrared spectral slopes, $\alpha_{3.6-8}$ and $\alpha_{3.6-24}$, vs. spectral type for all the sources with spectroscopic observation in the field of the NAP region. In each panel, the open gray circles show the diskless stars, and the filled circles are for the sources with infrared excess emission according to their $\alpha_{3.6-8}$ (top panel) and $\alpha_{3.6-24}$ (bottom panel). The red plus symbols mark likely asymptotic giant branch stars identified by their spectral features and their locations in the Hertzsprung–Russell (H-R) diagram. The dashed line shows the infrared spectral slope of the photospheric emission calculated with the BT-Settl atmospheric models, and the dotted lines are the 1σ standard deviation, assuming a 10% uncertainty in the Spitzer photometry.

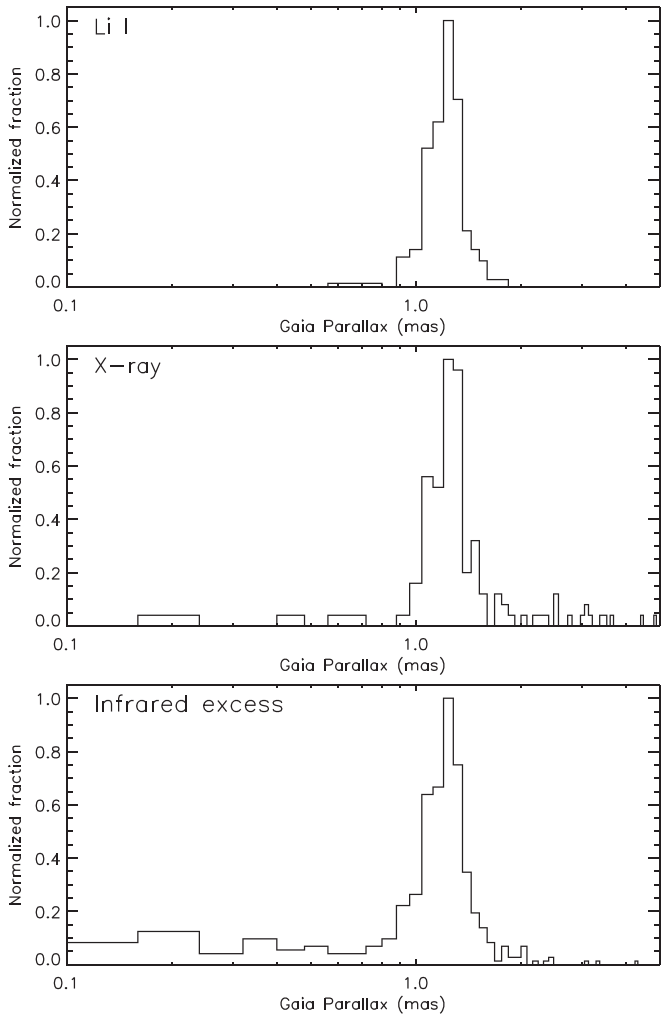

Figure 11. Distribution of Gaia parallax for the sources with Li I absorption (top), with X-ray emission (middle), and with infrared excess emission (bottom).

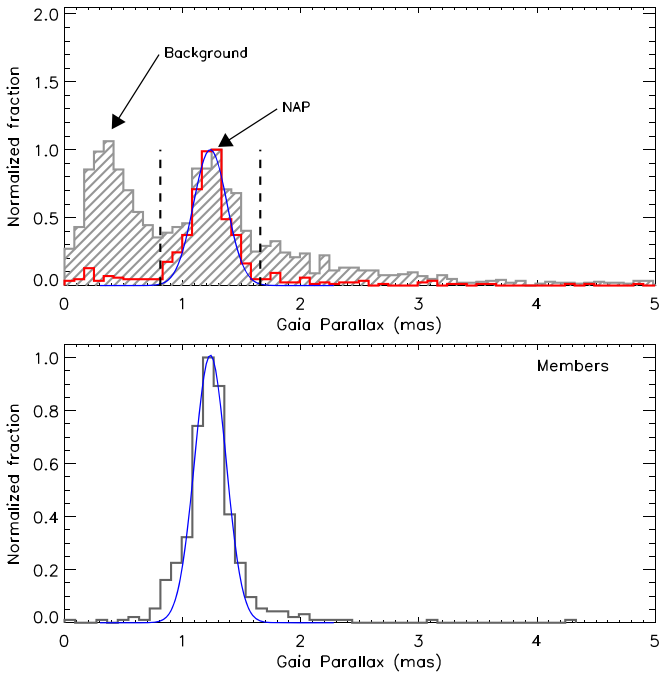

Figure 12. Top: distribution of Gaia parallax for our spectroscopic targets (gray hatched histogram) and the YSO candidates (red open histogram) before membership refinement. Bottom: distribution of Gaia parallax for the identified members after membership refinement in the NAP.

Spitzer photometry. Sources with infrared spectral slopes steeper than the slopes of the atmospheric models are considered as showing no infrared excess emission. For those with shallower infrared spectral slopes than the atmospheric models, we visually examine their SEDs. Sources that show infrared excess at a more than 3σ confidence level are considered to show infrared excess emission.

There are 518 sources that show infrared excess emission. An additional 6 sources show strong infrared excess, but their optical spectra are highly veiled and thus they cannot be classified. As they are likely true infrared excess sources, we include them for further investigation. Thus, in total, we identify 524 sources with infrared excess emission among our spectroscopic sample.

5.3.4. Gaia Astrometry

Combining the sources identified in the previous subsections having infrared excess emission, Li I absorption, or X-ray emission results in 655 unique YSO candidates. In this section, we further assess the likelihood of their membership in the NAP using the information from Gaia DR2 (Gaia Collaboration et al. 2016, 2018). Gaia astrometry can also reveal more members of the NAP that are not identified using the above three criteria. It is expected that the infrared excess and X-ray emission samples may be incomplete and that the Li I λ6708 indicator is not always apparent at our relatively low spectral resolution.

To control for only high-quality Gaia parallaxes, we compute the renormalized unit weight error (RUWE) following the method described in the Gaia DR2 manual. When RUWE > 1.4, it may indicate that the source is a multiple system, or may otherwise be problematic in terms of the astrometric measurement. In Figure 11, we show the distribution of Gaia parallaxes with RUWE $\leqslant 1.4$ for our YSO candidates selected using the above three criteria. The parallax distribution in each case strongly peaks at $\sim$1.24 mas. In the figure, we can note that the YSO candidates with infrared excess emission are contaminated mainly by background sources with small parallaxes, but the X-ray sample is polluted more by foreground sources; YSO candidates with identified Li I absorption represent the sample with the cleanest parallax distribution and thus the best sample of likely members of the NAP.

In Figure 12 we show the distribution of Gaia parallaxes with RUWE $\leqslant 1.4$ for all of our spectroscopic sample. Unlike the distributions shown in Figure 11, the parallax distribution for the full sample shows a double peak. This is due to background field stars at small parallaxes and the clustered NAP members. We combine the YSO candidates identified with the above three criteria and obtain the distribution of Gaia parallaxes with RUWE $\leqslant 1.4$ highlighted in red in the upper panel of Figure 12. We fit this distribution with a Gaussian function, limiting the fitting range to between 1.0 and 1.7 mas so as to reduce probable contamination. The fitting gives three parameters: $a_0 = 1.000$ is for the normalization, $P = 1.234$ mas is the centroid, and a standard deviation in the parallax $\sigma = 0.141$ mas. Hereafter, we adopt 810 pc as the distance of the NAP, consistent with the 795 pc value from Kuhn et al. (2020). For the YSO candidates

with Gaia parallaxes within $P - 3 \times \sigma$ and $P + 3 \times \sigma$, we accept them as members of the NAP. For those outside the limits of the parallaxes, we further inspect their membership as follows.

Li I absorption. Among the 350 YSO candidates identified with Li I absorption, 284 sources are within the established parallax limits. Of the other 66 sources, 26 have no estimate of parallax or a negative parallax is reported. We thus inspect their membership likelihood by considering their locations in the H-R diagram assuming they have a parallax of 1.234 mas and using the nonmagnetic evolutionary tracks from Feiden (2016) as a comparison (hereafter we only use these evolutionary tracks). We include all of them as members of the NAP based on their locations in the H-R diagram. For the other 40 sources, 33 have RUWE $>$ 1.4 and thus have unreliable astrometric measurement. We therefore continue to include them as member candidates. For the 7 sources with RUWE $\leqslant$ 1.4, 4 agree with the mean parallax of the NAP (1.234 mas) within $3 \times \sigma_{\rm plx}$, where $\sigma_{\rm plx}$ is the individual uncertainty on the parallax for each source. These sources are thus also considered as possible member candidates of the NAP. For the remaining 3 sources, an inspection of their SEDs suggests they show infrared excess emission, which is consistent with their being young stars but also allows the possibility that they could be lithium-rich, dusty giants. In Figure 13 (top), we show the H-R diagram for all YSO candidates identified with Li I absorption adopting a distance of 810 pc. For these three sources, their locations in the H-R diagram are consistent with other young stars. Thus, we list them as potential members of the NAP with a note indicating they could be excluded as members by our formal parallax criterion. In Figure 13 (top), we also note two sources are below the 10 Myr isochrone. While this is unusual, it could be the case that these sources harbor an edge-on disk and thus have their luminosities underestimated. In summary, we identify 350 likely members of the NAP with Li I absorption.

X-ray. In our spectroscopic sample, we find 175 counterparts for the X-ray sources. Among them, 106 also present Li I absorption and have already been included above as members of the NAP. For the remaining 69 sources, 36 are within the parallax limits we have established for the NAP, while 2 have no estimate of parallax or a negative parallax, 4 have RUWE $>$ 1.4, and 1 agrees with the mean parallax of the NAP (1.234 mas) within $3 \times \sigma_{\rm plx}$. We include all the aforementioned 43 sources as member candidates for further inspection of their SEDs and their locations in the H-R diagram. Among the 43, 11 sources do not show infrared excess emission and have H-R diagram locations consistent with those of main-sequence field stars. One star, known as LkHα 170 or V751 Cyg, which shows infrared excess and has been misclassified as a Herbig Ae/Be star, is an apparent VY Scl star (Greiner et al. 1999). A detailed description of this source is presented in Appendix C. The remaining 31 sources should be good members of the NAP, 15 of which show infrared excess emission. Among the 69 sources mentioned above, 43 have been accounted for, leaving 26 remaining sources that have RUWE $\leqslant$ 1.4 but are outside of the established limits on the parallax. Of these, 24 should be foreground/background field stars based on their locations in the H-R diagram. For the other 2, both of them should be young stars based on their locations in the H-R diagram: one has spectral type A8 and the other has spectral type M3, with extinction $A_V = 3.2$ mag, which is consistent with the other members. Thus, we include the M-type star as a member of the NAP. The A-type star has nonmeasurable extinction and is thus considered a foreground star. In conclusion, we confirm 32 members of the NAP based on the X-ray data. The middle panel of Figure 13 shows the H-R diagram for the members identified with X-ray emission.

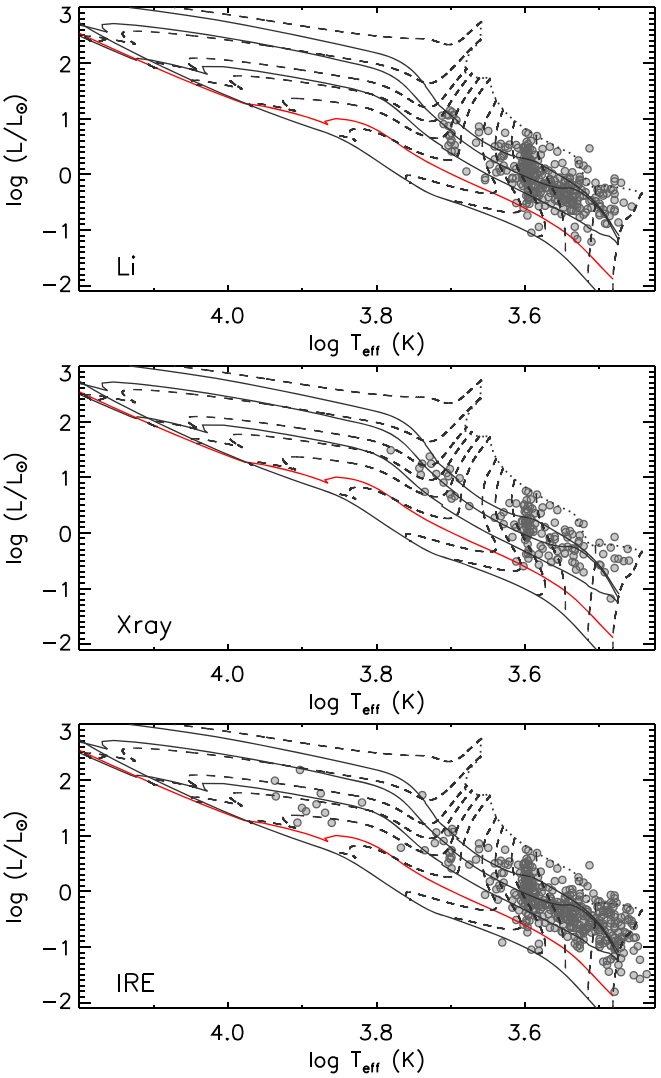

Figure 13. H-R diagram for young stars identified with Li I absorption (top), infrared excess (middle), and X-ray (bottom). The stellar luminosity is derived from fitting the SEDs using model atmospheres. In each panel, the nonmagnetic evolutionary tracks (dashed lines) from Feiden (2016) are shown as a comparison. The solid lines show the isochrones at ages of 0.5, 1, 3, 5, 10, and 50 Myr from top to bottom. The dotted line connecting the tops of the mass tracks indicates the birth line. The dashed lines present the evolutionary tracks of YSOs with masses of 0.09, 0.2, 0.4, 0.6, 0.8, 1.0, 1.5, 2.0, 2.5, 3.0, 4.0, and 5.8 $M_{\odot}$.

Infrared excess. Among the 524 YSO candidates with infrared excess emission, 289 sources have been identified as members of the NAP above, based on Li I absorption and/or X-ray emission. Among the remaining 235 sources, 120 are within the parallax limits we have established for the NAP, 35 have no estimate of parallax or negative parallaxes, 18 have RUWE $>$ 1.4, and 23 agree with the mean parallax of the NAP (1.234 mas) within $3 \times \sigma_{\rm plx}$. Among the 196 total sources, 6 sources have strong infrared excess and highly veiled spectra. For these, we visually inspect their locations in the H-R diagram and identify 164 sources as likely members of the NAP. For the six sources with highly veiled spectra, we cannot place them in the H-R diagram since their spectra cannot be

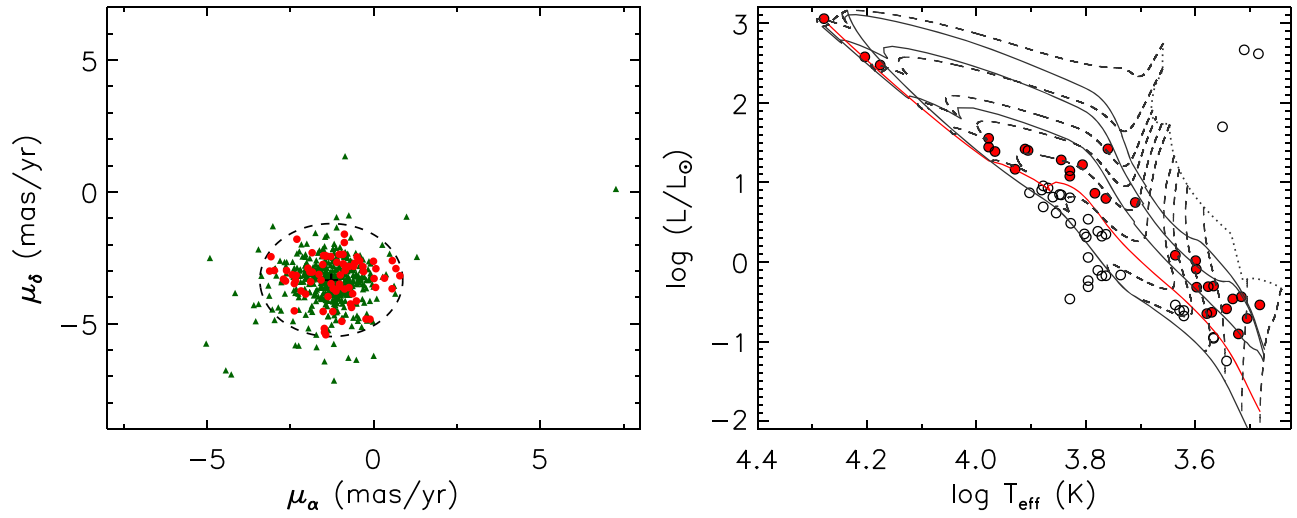

Figure 14. Left: Gaia proper motions of members (green filled triangles) identified with Li I absorption, X-ray emission, and/or infrared excess emission. Only the members with RUWE $\leqslant$ 1.4 are used for the plot. The mean proper motions of the members and the 3σ ellipses of the standard deviation of the distribution are shown with a dashed-line curve. The red filled circles are the member candidates selected based solely on their parallaxes and proper motions. Right: H-R diagram for sources identified as members based solely on their Gaia parallax values with stellar luminosities calculated adopting the mean distance of the NAP (810 pc). Sources (red filled circles) apparently younger than 10 Myr are selected as members, and others (open circles) are considered as field stars with distances close to that of the NAP. The evolutionary tracks are the same as in Figure 13.

classified. We simply include them as probable members of the NAP. For the other 39 sources, 2 of them might be members of the NAP based on their locations in the H-R diagram. In total, we identify 172 members of the NAP based on infrared excess emission. We also find that 40 nonmembers with spectral types earlier than G show infrared excess emission; they are presented in Appendix B. The bottom panel of Figure 13 shows the H-R diagram for the members identified with infrared excess emission.

New Gaia members. Besides the 554 members identified with the above three criteria, we also consider as candidate members of the NAP sources with spectroscopic observations that are within $P - 3 \times \sigma$ and $P + 3 \times \sigma$ of the nominal parallax and that have proper motions consistent within 3σ of the mean proper motion (see the left panel of Figure 14). In this way, we obtain 62 additional candidates among our spectroscopic sample. We further consider their membership likelihood using the H-R diagram and select only those apparently younger than 10 Myr as members. In the right panel of Figure 14, we show these 26 newly appreciated members, as well as the other 36 field stars with distances close to that of the NAP.

In summary, by considering the three samples selected on the basis of YSO criteria in the last section, plus additional sources with kinematics consistent with those of stars meeting the YSO criteria, we have identified a total of 580 members of the NAP from our spectroscopic sample. Among them, 461 show infrared excess emission and are likely disk-bearing young stars, while the other 119 sources do not show infrared excess emission (based on available Spitzer data). The criteria by which the individual members are identified are given in Table 4. The distribution of the parallax for these sources (restricted to RUWE $\leqslant$ 1.4) is shown in the bottom panel of Figure 12. A Gaussian fit to the distribution of the parallax also gives a mean distance of ~810 pc. The spatial distribution of all the spectroscopically identified members of the NAP is shown in Figure 1; while the Bajamar Star and HD 199579 are illustrated there, we note that our spectroscopic survey does not cover the immediate vicinity of either of these two massive O-type stars in the region.

5.4. Optical Photometric Variability

While we do not use variability as a selection criterion for cluster membership, discussed above in Section 5.3, we do assess the implications of photometric variability on the H-R diagram in Section 6.3. We identify variable stars among our spectroscopic sample in the following way.

First, we extract the light curves for all stars with Gaia distances < 2 kpc in the NAP field from the ZTF survey. For each star, we consider its photometry only between the 95th and 5th percentile points in the r-band light curve, in order to exclude the possibility of contamination from bad pixels, cosmic rays, spurious measurements, etc. For those stars with at least 30 measurements, we then calculate the standard deviations (σ_r) and mean ($\bar{r}$) of the selected photometric measurements.

In Figure 15, we show σ_r as a function of $\bar{r}$ for those stars. Then, we divide $\bar{r}$ into different magnitude bins with a bin size of 0.2 mag and calculate the 3σ-clipping mean ($\overline{\sigma}_r$) of σ_r for all the stars in each magnitude bin. In Figure 15(a), we also show the relation between $\overline{\sigma}_r$ and $\bar{r}$. It is expected that $\overline{\sigma}_r$ increases toward fainter $\bar{r}$, which is indeed seen at $\bar{r} \gtrsim 13.2$ mag. However, the relation is inverted when $\bar{r} \lesssim 13.2$, which may be due to saturation (the saturation limits lie within ~12.5 to 13.2 mag in the r band). Thus, in this work, we only investigate the variability of stars with $\bar{r}$ fainter than 13.2 mag. Next, we interpolate the $\overline{\sigma}_r$–$\bar{r}$ relation for different $\bar{r}$ and define those with $\sigma_r > 3\overline{\sigma}_r$ as strongly variable stars, those with $3\overline{\sigma}_r \geqslant \sigma_r > 2\overline{\sigma}_r$ as moderately variable stars, and those with $\sigma_r \leqslant 2\overline{\sigma}_r$ as weakly variable stars.

Among the 503 members of the NAP, as defined in Section 5.3, based on an estimate of their variability from ZTF, 53.5% show high variability (>3σ) and an additional 15.7% are moderate variables (2–3σ). The fraction of highly variable members is 60.4% for those YSOs showing infrared excess emission and only 28.8% for those without infrared excess emission. For the stars in the general field of the NAP,

Table 4
Young Stars in the NAP

ID	R.A. (J2000)	Decl. (J2000)	Adopted SPT	r_{7465}	Q[a]	$T_{\rm eff}$ (K)	Model[b]						X-shooter Template[c]						YSO Criteria[d]			
							Fixing r_{7465}		Varying r_{7465}		Adopted		Fixing r_{7465}		Varying r_{7465}		Adopted					
							A_V (mag)	$L_\star$ ($L_\odot$)	A_V (mag)	$L_\star$ $L_\odot$)	A_V (mag)	$L_\star$ $L_\odot$)	A_V (mag)	$L_\star$ ($L_\odot$)	A_V (mag)	$L_\star$ $L_\odot$)	A_V (mag)	$L_\star$ $L_\odot$)	IRE	Li	X-Ray	Var
1	20 48 50.71	+43 49 49.7	Cont	High	…	…	…	…	…	…	…	…	…	…	…	…	…	…	Y	…	…	H
2	20 49 11.78	+44 12 32.9	K7.0	0.00	1	3970	3.9	1.489	3.9	1.489	3.9	1.489	3.8	1.320	3.8	1.320	3.8	1.320	Y	Y	…	H
3	20 49 14.47	+44 14 49.9	M4.8	0.00	1	3015	2.0	0.217	2.1	0.224	2.0	0.217	1.6	0.175	1.6	0.175	1.6	0.175	Y	Y	…	L
4	20 49 20.30	+44 35 13.5	M2.4	0.00	1	3437	2.4	0.387	2.4	0.387	2.4	0.387	2.5	0.359	2.5	0.359	2.5	0.359	Y	Y	…	L
5	20 49 24.76	+44 35 21.8	M5.6	0.00	1	2908	1.9	0.174	2.3	0.201	1.9	0.174	0.8	0.097	0.8	0.097	0.8	0.097	Y	…	…	L
6	20 49 32.19	+44 17 03.1	M1.2	0.18	1	3602	2.5	0.671	2.0	0.614	2.3	0.643	2.6	0.718	2.1	0.587	2.4	0.653	Y	Y	…	H
7	20 49 53.51	+44 10 17.3	M3.4	0.00	1	3279	0.1	0.106	0.3	0.114	0.1	0.106	0.0	0.095	0.0	0.095	0.0	0.095	N	Y	…	L
8	20 50 06.05	+44 17 49.0	M4.0	0.00	1	3160	1.4	0.467	3.3	0.713	1.4	0.467	1.0	0.344	1.0	0.344	1.0	0.344	N	Y	…	H
9	20 50 09.92	+44 15 21.3	M1.4 ± 0.0	0.00	1	3573	3.0	0.412	3.3	0.434	3.0	0.412	3.2	0.399	3.4	0.413	3.2	0.399	Y	Y	…	H
10	20 50 22.43	+44 19 17.6	M4.0 ± 0.0	0.19	1	3160	4.1	0.635	4.6	0.694	4.4	0.665	3.8	0.586	4.5	0.588	4.1	0.587	Y	…	Y	L
11	20 50 27.71	+44 23 29.1	K3.8	0.49	2	4374	2.9	2.805	2.6	3.551	2.7	3.178	3.0	4.363	2.8	4.072	2.9	4.218	Y	Y	…	M

Notes.
[a] Ranking for the spectral classification: 1 for very good, 2 for fair, and 3 for poor.
[b] Fitting the SEDs of young stars with model atmospheres. Fixing r_{7465}: during the SED fitting, the r_{7465} is fixed to be the one derived from the spectral classification; Varying r_{7465}: r_{7465} is a free parameter during the SED fitting.
[c] Fitting the SEDs of young stars with X-shooter templates. Fixing r_{7465} and Varying r_{7465} are the same as for [b].
[d] IRE: showing infrared excess; Li: showing Li I λ6708 absorption; X-ray: having an X-ray counterpart; var: H for highly variable, M for moderately variable, and L for weakly variable (see Section 5.4).

(This table is available in its entirety in machine-readable form.)

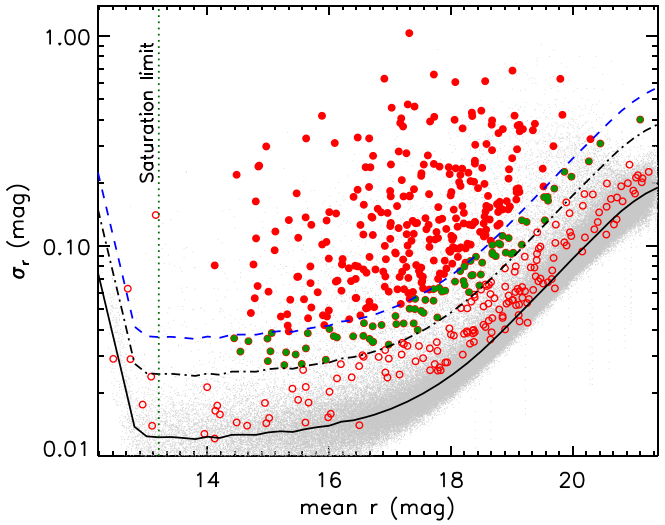

Figure 15. Photometric variability statistic σ_r vs. mean magnitude $\bar{r}$ for all stars in the NAP field with distance less than 2 kpc. The underlying distribution is shown as small gray dots. The black solid line marks $\overline{\sigma}_r$ within the individual magnitude bins, while the black dashed–dotted line indicates $2 \times \overline{\sigma}_r$ and the blue dashed line $3 \times \overline{\sigma}_r$. The YSOs we have identified are shown as circles: red filled circles are for strongly variable stars, green filled circles for moderately variable stars, and open circles for stars with low variability.

as shown in Figure 15, but not necessarily members of the young cluster, only 1.0% are highly variable, and 1.3% are moderately variable. The classification of variability for individual members is listed in Table 4.

6. Results on the Stellar Population of the NAP

6.1. Properties of the Final Catalog of Stellar Parameters

Among our large spectroscopic sample, we have identified 580 members of the NAP, and we obtain the spectral types of 574 of these sources. Figure 16 shows the distribution of the spectral types, veiling values, and extinction values derived for these sources using the methods described in Sections 5.1 and 5.2.

In the top panel of Figure 16, the spectral types of the members are compared to a calculated distribution of spectral types for model clusters having ages of 1 and 10 Myr and the mass function derived in the Trapezium cluster (Muench et al. 2002). Assuming that the NAP and Trapezium clusters have a similar mass function, we can search for biases in our spectroscopic survey. As shown in Figure 16, our sample includes more sources with spectral type between F0 and A0 than the 1 Myr model cluster, suggesting that our sample is substantially incomplete for the middle-M and later spectral types. The 10 Myr model cluster predicts a distribution of stars with spectral type between F0 and A0 that is more similar to that of the observed NAP, but also has many more stars that are earlier than A0 than the observed NAP.

The middle panel of Figure 16 shows the distribution of r_{7465} derived from our spectral classification. Among the 484 disk-bearing YSOs, 46.5% (225/484) show measurable veiling on top of their absorption spectra. The median r_{7465} is around 0.4 with a tail to higher values. The bottom panel of Figure 16 shows the distribution of visual extinction. The peak value is $A_V = 2.6$ mag with a tail extending to about 10 mag.

The top panel of Figure 17 shows that there is no correlation between the derived veiling values, r_{7465}, and the spectral

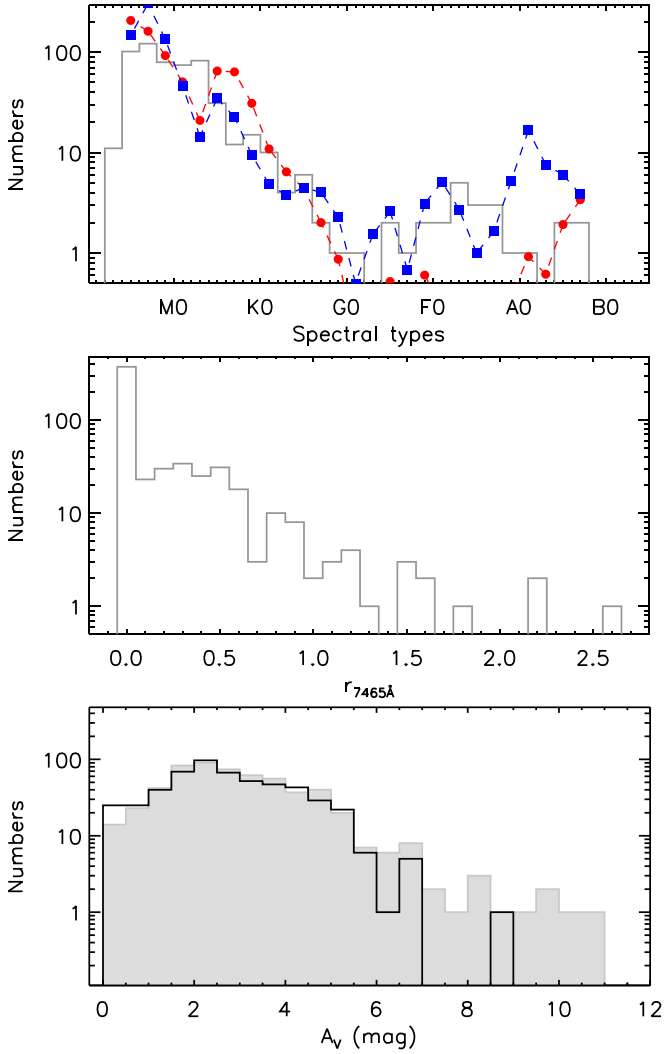

Figure 16. Results of our spectral and SED fitting processes for members of the NAP. Top: distribution of spectral types. The red dashed line connecting filled circles shows the predicted distribution of spectral types for a 1 Myr model cluster with an initial mass function like that of the Trapezium cluster, while the blue dashed line connecting filled boxes is for a 10 Myr model cluster. Middle: distribution of veiling at 7465 Å. Bottom: distribution of V-band extinction, derived from fitting SEDs using model atmospheres (gray filled histogram) or X-shooter templates (black open histogram).

types, SpT. The bottom panel of Figure 17 shows A_V versus spectral types. While there is, reassuringly, no correlation between A_V and spectral types in our sample, there are 12 M-type sources with $A_V \lesssim 0.5$ mag, which is much smaller than those of other members. The extinction of these 12 sources could be underestimated due to the discrepancy between their SEDs and the templates used for SED fitting at these late spectral types.

For placing stars in the H-R diagram, we have adopted A_V and $L_\star$ from the SED fitting using model atmospheres for YSOs with spectral types earlier than K0 and using X-shooter templates for those YSOs with later spectral types. In Table 4, we list the parameters derived from each method and the value we adopt.

Finally, in Figure 18, we show the H-R diagram for the entire set of NAP members identified among our spectroscopic sample, compared with the nonmagnetic evolutionary tracks from Feiden (2016). Their B2 to M7 distribution of spectral

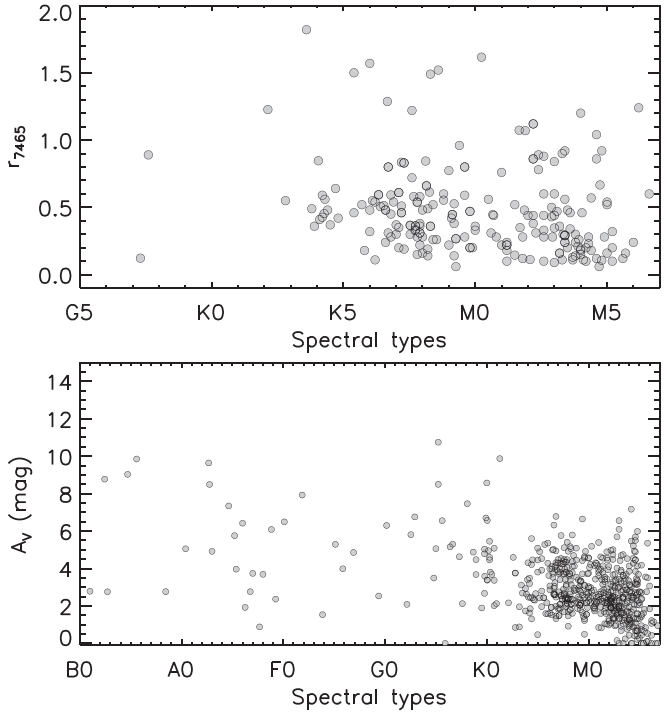

Figure 17. Veiling (top) and visual extinction (bottom) as a function of spectral type for the members of the NAP. The top panel includes only the subsample with measurable veiling in the spectra, while the bottom panel includes all members of the NAP studied in this work.

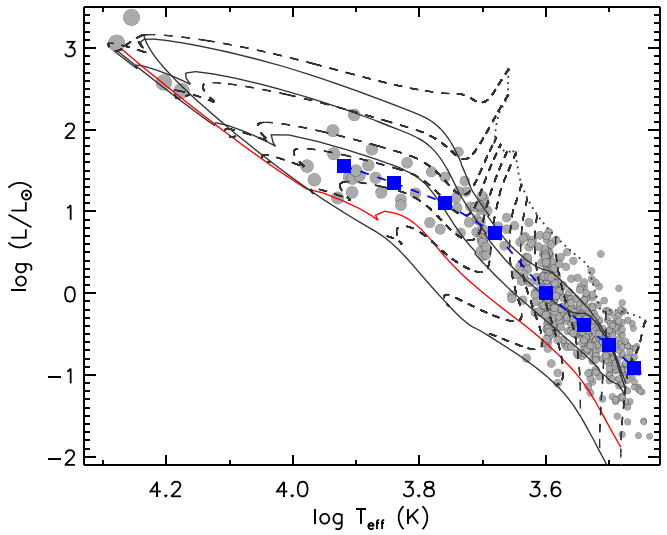

Figure 18. H-R diagram for the members (gray filled circles) of the NAP. The sizes of the circles are scaled with the $T_{\rm eff}$ of the sources. The evolutionary tracks are the same as in Figure 13.

types corresponds to stellar masses ranging from >5.8 $M_{\odot}$ to <0.09 $M_{\odot}$. The luminosity range of the main locus spans ages of about 0.5–5 Myr.

We divide the NAP members into different log $T_{\rm eff}$ bins and estimate the median luminosity and the luminosity dispersion. The result is listed in Table 5 and also shown in Figure 18. The comparisons with model evolutionary tracks suggest a median age of ∼1 Myr for the NAP members. Following Hillenbrand et al. (2008), we use the median luminosity as a function of temperature, as plotted in the figure, to characterize the overall stellar population. Below, we compare this median H-R diagram for the ensemble population to different subpopulations of stars, including kinematic subclusters of the NAP complex, and certain categories of stars such as variable objects.

Table 5
The Median Luminosity and Luminosity Dispersion of Young Stars within Individual $T_{\rm eff}$ Bins

Log $T_{\rm eff}$ (K)	Median Log $L_{\star}$ ($L_{\odot}$)	σLog $L_{\star}$ ($L_{\odot}$)
3.96–3.88	1.560	0.325
3.88–3.80	1.350	0.288
3.80–3.72	1.106	0.377
3.72–3.64	0.732	0.309
3.64–3.56	0.008	0.348
3.56–3.52	−0.391	0.286
3.52–3.48	−0.638	0.340
3.48–3.44	−0.913	0.390

6.2. The H-R Diagram for Different Kinematic Groups

Kuhn et al. (2020) investigated the kinematics of young stars in the NAP region using the data from Gaia DR2. They confirmed 395 previously identified young stars with reliable astrometric measurements as cluster members and divided them into six groups, which we show in Figure 19. Among the 395 sources, we have obtained spectral types for 302 sources and included 299 as members of the NAP based on the analysis described in Section 5.3. For the remaining 3 sources, they do not show infrared excess emission and have isochrone ages older than 10 Myr and are thus excluded as members of the NAP. The majority of the 299 YSOs are in Groups C, D, E, and F.

Besides the YSOs that are already grouped, we have 316 members in our sample without assigned groups from Kuhn et al. (2020). We tentatively assign these stars to groups based on their spatial locations. In Figure 19 we depict the boundaries of Groups C, D, E, and F using four ellipses. Groups E and F are spatially separated, and the ungrouped YSOs near them can be easily divided into individual groups based on their locations. Groups C and D overlap, and it is hard to assign a group without reliable kinematic data. To avoid potential contamination, we only use the kinematic members identified by Kuhn et al. (2020) in the case of Group C and include only the ungrouped YSOs within the boundary of Group D but outside of the boundary of Group C as members of Group D. In this way, we have 43, 383, 89, and 15 YSOs in Groups C, D, E, and F, respectively.

In Figure 20 we show the H-R diagram for the four kinematic groups. We judge the relative ages of individual groups by comparing their H-R diagrams with the median locations of all the members of the NAP (Figure 18). In the H-R diagram, 62% of the members in Group C, 46% in Group D, 54% in Group E, and 27% in Group F are above the median locations of the members of the NAP, indicating that Groups C and E are younger than Group D, while Group F is the oldest. Groups A and B have only four and eight stars with spectroscopic data, respectively, with only two stars in Group A and three stars in Group B that are above the median location of the members of the NAP. Given such small numbers of members in both groups, it is hard to judge the relative ages among the groups; all we can say is that they have ages comparable to those of other groups in the NAP region.

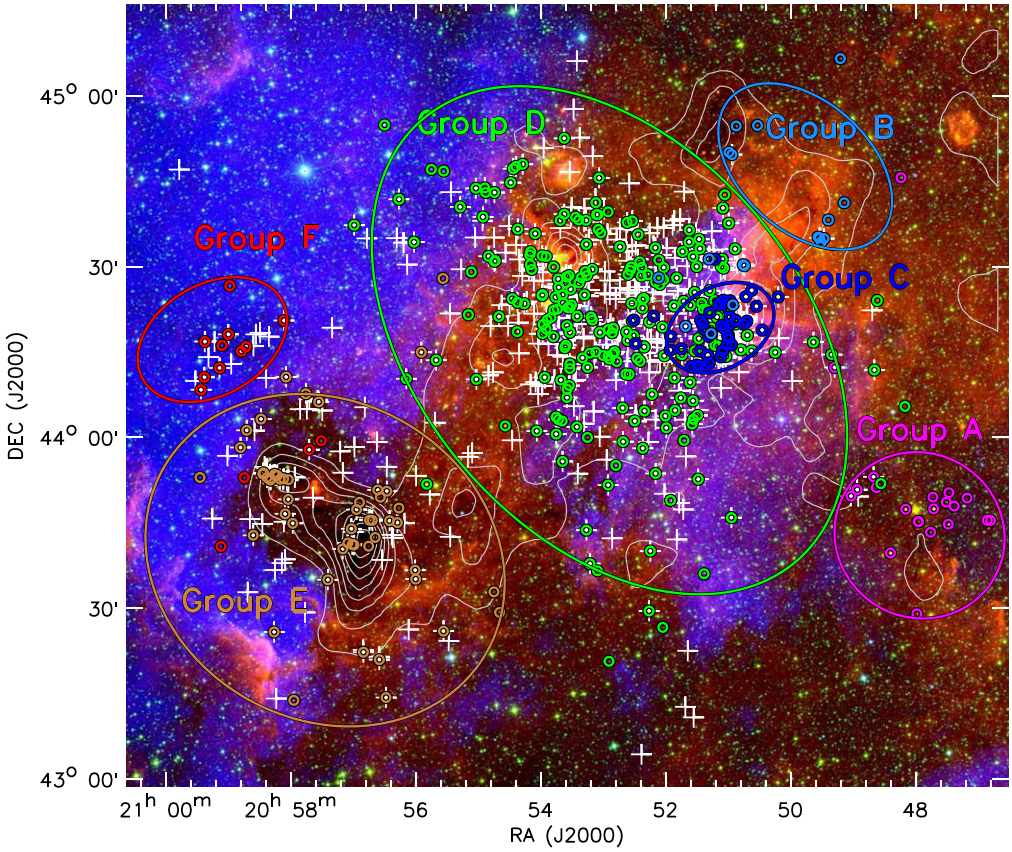

Figure 19. NAP members (white pluses) identified in this work overplotted on a three-color image of the North America Nebula created in the same way as in Figure 1. The color-coded open circles are members of the individual kinematic groups identified by Kuhn et al. (2020). The color-coded large ellipses show the boundaries of the kinematic groups depicted in this work to group the YSOs without reliable astrometric measurements.

6.3. The H-R Diagram and Stellar Variability

In Section 5.4, we have investigated the variability of the members of the NAP and divided them into three categories: high, moderate, and low r-band photometric variability. In Figure 21, we show the H-R diagrams for the YSOs with different amplitudes of variability. A similar luminosity spread can be noted in YSOs with low to high variability.

To quantify this impression, we first limit $T_{\rm eff}$ between 3000 and 4000 K to calculate the luminosity spread. We then fit the log $L_\star$–log $T_{\rm eff}$ relation with a linear function and then subtract the calculated log $L_\star$ at log $T_{\rm eff}$ using the fitted linear function. In this way, we can remove the contribution in the luminosity spreads from the general slope of the log $L_\star$–log $T_{\rm eff}$ relation. The luminosity spreads are then calculated using the resulting residual luminosity as 0.32, 0.24, and 0.31 dex for YSOs with low, moderate, and high variability. The luminosity spreads are similar for YSOs at low and high variability. The lower luminosity spread for the moderately variable YSOs may be attributed to the relatively smaller number of sources in this category.

7. Discussion

7.1. The Effect of Spectral Veiling on Stellar Classification

Figure 4 shows that a veiling continuum superposed on the absorption spectra of young stars can affect the spectral classification process. Among the 224 sources in our sample with measurable veiling in their optical spectra, the spectral types that result from fitting the spectra with a veiling component included are systematically later than those derived without accounting for veiling. The size of the effect is typically ∼1.2 subclasses later for spectral types later than K7 and ∼4.2 subclasses later for earlier types. For any individual source there will be a dependency on the veiling flux itself; the numbers quoted above can be considered appropriate for a typical veiling value $r_{7465} \approx 0.4$ as illustrated in the distribution of Figure 16.

How does the presence of veiling shift the location of young stars in the H-R diagram? To investigate this quantitatively, we refit the SEDs of the member stars in our sample to derive their stellar luminosity adopting the spectral type from fitting the spectra without consideration of veiling.

We find that there are no systematic shifts in the stellar luminosity in fitting the SEDs with veiling or without veiling. This can be understood to be due to the fact that although there is an obvious effect on the temperatures, there is also a trade-off between temperature shift and bolometric correction shift, extinction correction shift, and veiling correction shift. In addition, the veiling effect is predominantly considered in the optical part of the flux distribution (or the Wien side, if considering a Planck function representation of the stellar atmosphere), which is still far from the peak flux in the red or near-infrared wavelength range. Regarding the temperatures, there is a much larger effect however. Due to the ∼1–4 subclass difference for the spectral types, the locations of the veiled young stars will systematically shift to hotter temperatures, typically by ∼130 K for stars with spectral types later than K7 and typically by ∼680 K for earlier-type stars. When

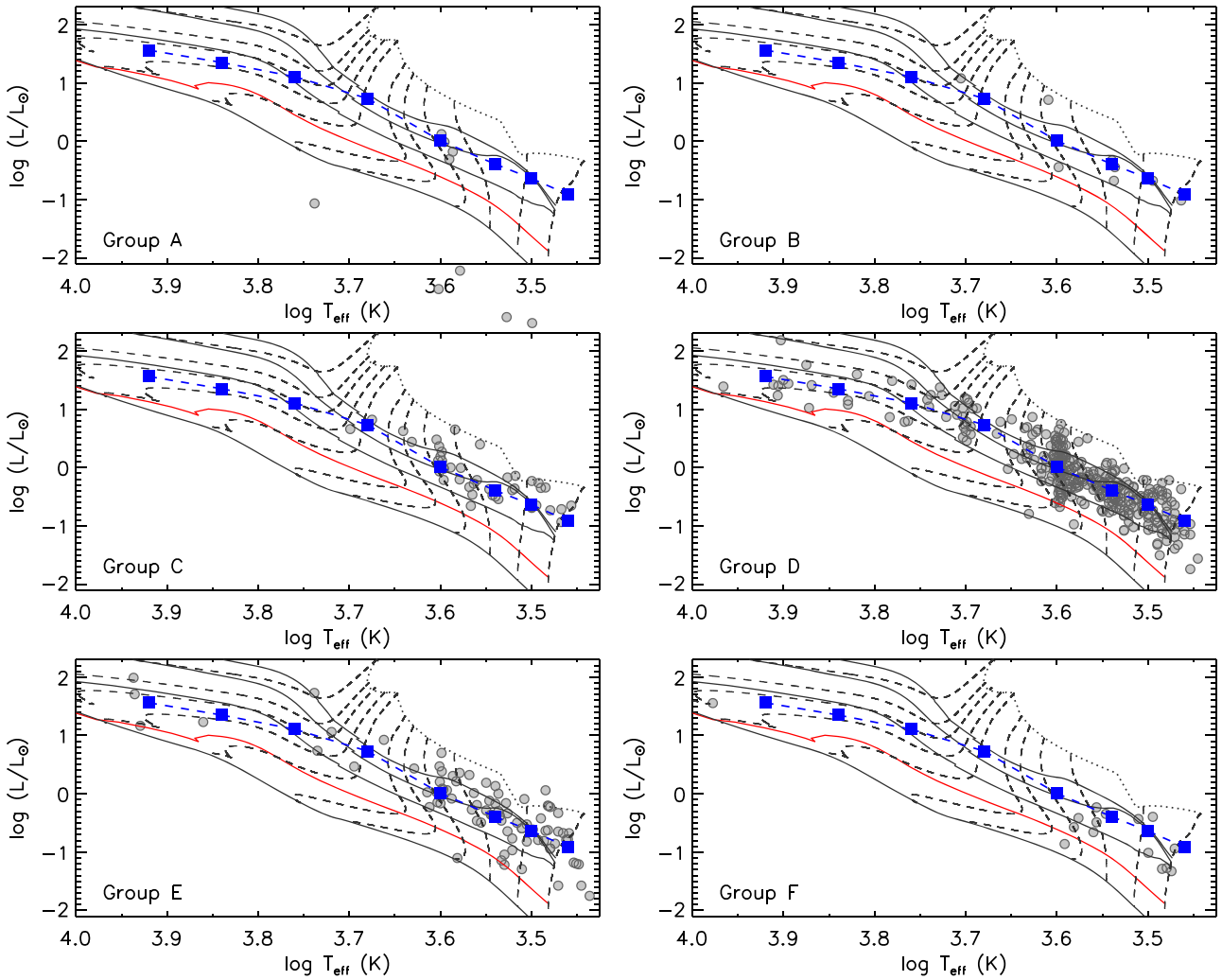

Figure 20. H-R diagram for YSOs in six kinematic groups identified by Kuhn et al. (2020). In each panel, the blue filled boxes linked by dashed lines are the median locations of the members of the NAP in the H-R diagram. The evolutionary tracks are the same as in Figure 13.

$L_\star$ stays the same, as $T_{\rm eff}$ gets hotter, the stellar radius also becomes smaller, so the stellar age is older when excluding veiling in the spectral classification. Thus, for the earlier spectral types especially, it is very important to include the potential effects of veiling when performing spectral classification.

We further test how wrong the spectral type could be with increasing veiling by taking the X-shooter templates and veiling them artificially, adopting a constant shape for the veiling continuum flux. The veiling effect is parameterized as r_{7465}, as used elsewhere in this work. We then follow the spectral classification procedure for these veiled spectra without consideration of veiling. As expected, the resulting spectral types tend to be earlier than the input ones. Figure 22 shows the difference between the input and resulting spectral types as a function of r_{7465}. When excluding veiling in spectral classification, for $r_{7465} \gtrsim 0.2$ the errors on the spectral types are generally larger for mid-K-type and early K–type stars than for M-type stars.

7.2. Veiling Variations

Young stars usually show variable accretion activity, which is a likely cause of the variable veiling on the spectra. As demonstrated in Figure 22, if we do not consider veiling in the spectral classification process, we would obtain potentially very different and erroneous spectral types for the stars. This effect may also be the cause for the discrepancy among reported spectral types in the literature for some young stars with substantial variable accretion activity.

In this work, we have identified 134 young stars that show measurable veiling in their optical spectra and have been observed spectroscopically at multiple epochs. In Figure 23, we show the ratio between the maximum and minimum of r_{7465} versus the mean r_{7465} for these sources. The median of the ratios between the maximum and minimum of r_{7465} is about 1.6. Among these sources, there is one (ID 425 or 2MASS J20573729+4406439) that shows a large mean r_{7465} (0.88) and a high ratio (11.57) between the maximum and minimum of r_{7465}. In Figure 24, we show four spectra of the object observed at different dates. Variation in the strength of the TiO absorption bands is prominent among these spectra. The spectra also show strong accretion-related emission lines, e.g., He I 5876 Å, 6678 Å, Hα, and the Ca II "infrared" triplet, all indicating strong accretion activity. The variations in the strength of the TiO bands, which are anticorrelated with changes in the emission line strength, are likely due to the

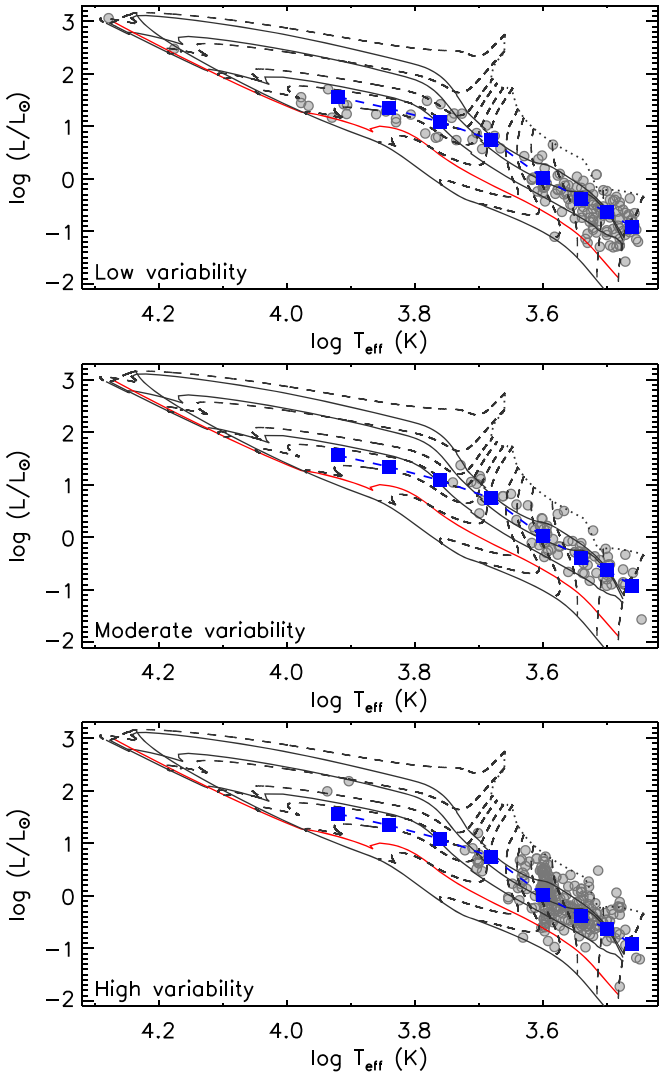

Figure 21. H-R diagram for young stars with photometric variability data, showing variability at low (top panel), moderate (middle panel), or high (bottom panel) levels. The evolutionary tracks are the same as in Figure 13.

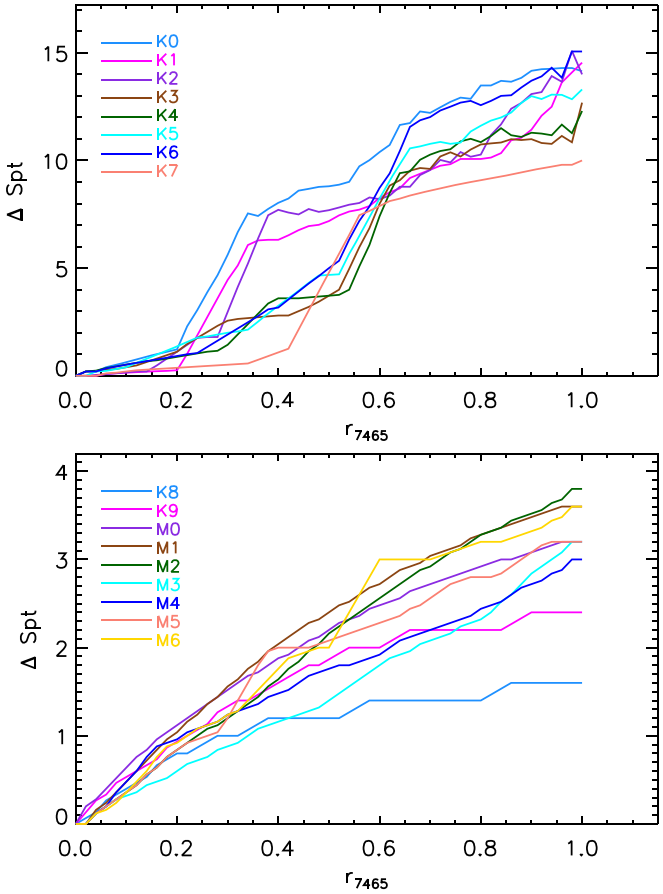

Figure 22. Difference between the input spectral types and the spectral types derived from the veiled spectra without the consideration of veiling as a function of veiling strength r_{7465}. Each colored line is for a different input spectral type.

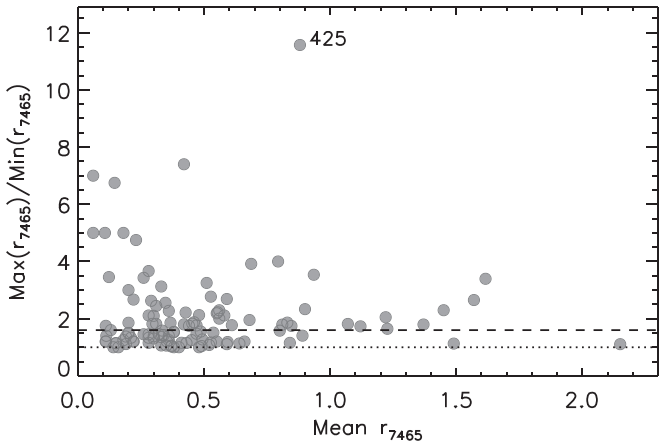

Figure 23. Ratio of the maximum to the minimum of r_{7465} vs. the mean r_{7465} for accreting young stars in our sample with multiple-epoch spectroscopic observations. The dotted line shows the equal ratio, and the dashed line shows the median of the distribution, which is 1.6. An outlier in the distribution, with both large mean veiling and large variability in the veiling, is Source 425 (2MASS J20573729+4406439); see Figure 24 for details.

variable excess emission induced by the accretion variability. When veiling is excluded in doing the spectral classification, the spectral type of the object can vary from K6 to M4.2 (see the top panel of Figure 24). The spectral types from different spectra converge when we include veiling in the spectral fitting (see the bottom panel of Figure 24). The source may represent an extreme case in our sample, but it is a perfect example for showing the importance of taking veiling into consideration when doing spectral classification.

For Source ID 425, assuming that the shape of the veiling continuum flux is constant, the change of r_{7465} from 0.14 to 1.88 would lead to a ∼0.8 mag brightness change in the r band, which is comparable to the maximum variation ($\Delta r = 0.9$ mag) observed in the r band from the ZTF survey. However, the ZTF survey did not cover the observation dates for our spectroscopic observations, which were earlier. However, the similar variations in recent photometry and older spectroscopy indicate that the accretion variations have continued for years and possibly decades. For a source with such strong variations in the photometry, it is necessary for accurate H-R diagram placement that the photometry is taken at the same time as the spectra in order to better characterize the stellar properties. Unfortunately, this is not the case for Source ID 425.

To quantify the impact of different, typically unknown accretion scenarios for H-R diagram placement, we can simulate the observations for a case like Source ID 425 and

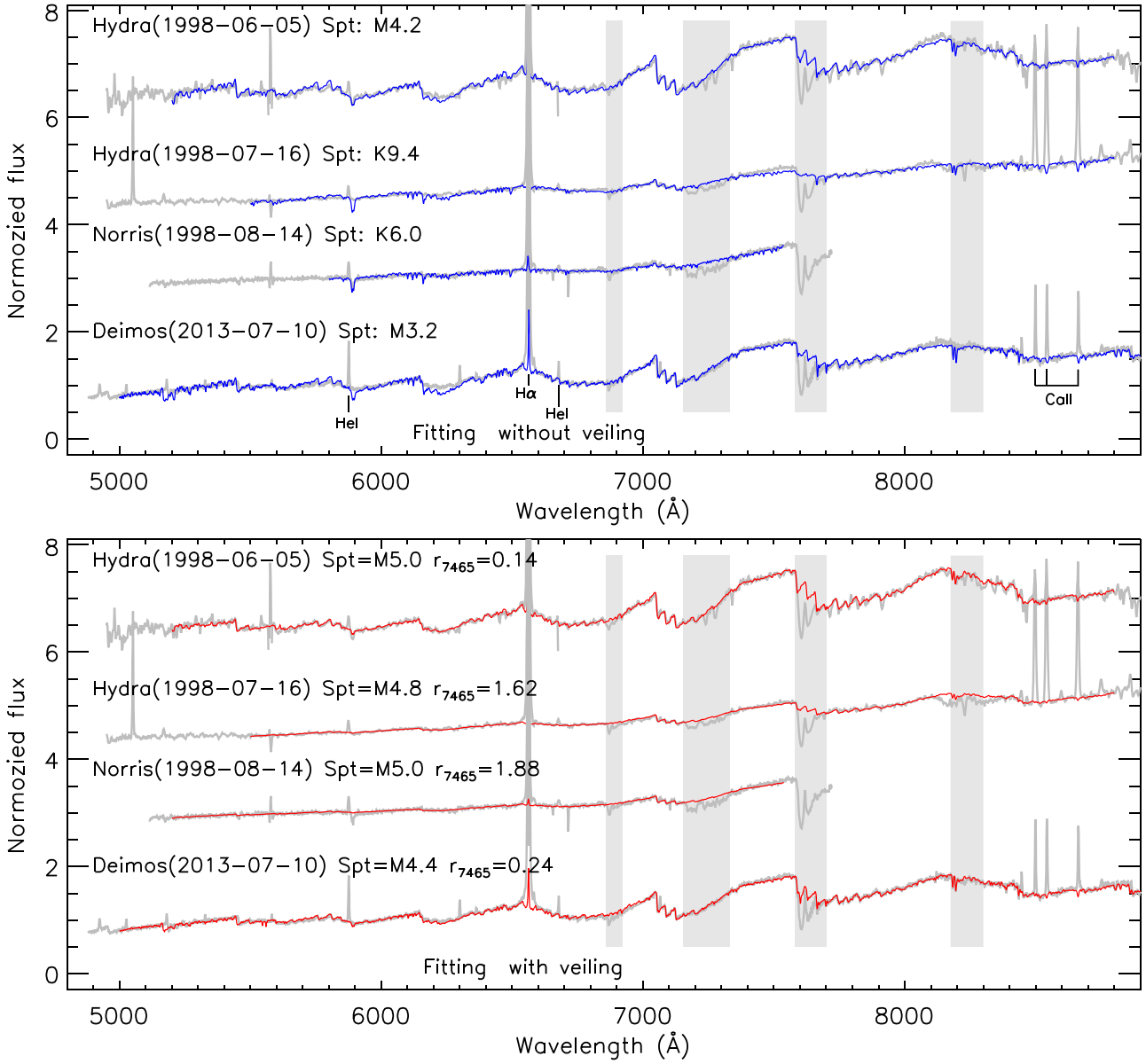

Figure 24. Illustration of the spectral template fitting for Source 425 (2MASS J20573729+4406439), which was observed with Hydra, Norris and DEIMOS and shows significant variations in the presented spectrum over time. The best-fit X-shooter empirical spectral templates (colored lines) are overplotted on the observed spectra (gray). Vertically oriented gray bars indicate regions masked due to potential contamination from telluric features. Fits without veiling (top panel) and with veiling (bottom panel) are shown. While the nonveiled templates produce a range of spectral type solutions, the veiled templates (bottom panel) produce a consistent spectral type with a large variation on the veiling parameter.

inspect how the input parameters and the derived parameters can differ. We consider an M5-type YSO with an age of 1 Myr and $A_V = 3$ mag. This YSO is modeled to exhibit variable accretion activity parameterized by r_{7465} that is varied from $r_{7465} = 1.6$ to $r_{7465} = 0.1$.

We model four cases. In the first two cases, we assume that both the broadband photometry and the spectra are observed simultaneously when $r_{7465} = 1.6$ (Case 1) or $r_{7465} = 0.1$ (Case 2), and we derive the stellar parameters without consideration of veiling. In Case 3, we assume the broadband photometry is taken when $r_{7465} = 1.6$, and the spectrum is observed when $r_{7465} = 0.1$. For Case 3, we derive the stellar parameters when neglecting or considering veiling in spectral classification. Case 4 is similar to Case 3 but assumes the photometry is taken when $r_{7465} = 0.1$ and the spectrum is obtained when $r_{7465} = 1.6$. For individual cases, the simulated results are shown in Figure 25. From the input $T_{\rm eff}$ and $L_\star$, the model star is expected to be 1 Myr old with a mass of 0.09 $M_\odot$. When excluding the veiling effect in spectral classification, the derived $T_{\rm eff}$ and $L_\star$ vary depending on r_{7465}, which induces large uncertainty in the estimated stellar masses and ages. In an extreme case, the derived mass and age can be 0.64 $M_\odot$ and 25 Myr, which are very different from the input 0.09 $M_\odot$ and 1 Myr. When including veiling effects in spectral classification, the derived mass is consistent with the input one, but the age measurement can be very uncertain, from 0.3 to 4 Myr. In the simulations, we have assumed that all broadband photometry is observed simultaneously, but this may not be the case in reality, which could induce additional uncertainties given that many YSOs are variable at the >0.05–0.1 mag level (see Section 5.4).

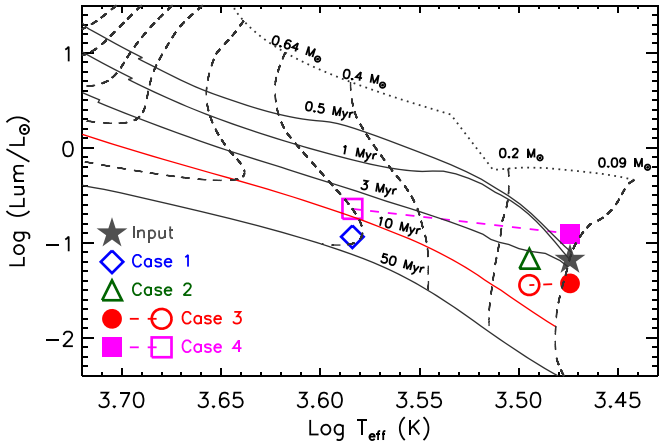

Figure 25. H-R diagram for a model star with $T_{\rm eff}$ and $L_{\star}$ derived from simulated observations in four hypothetical cases. The gray filled star symbol marks the location of the model star with the input $T_{\rm eff}$ and $L_{\star}$. We perform four simulations and assume that the photometry and spectra are taken simultaneously for two cases (Cases 1 and 2) and not for the other two (Cases 3 and 4). In Cases 1 and 2, the data are assumed to be taken with $r_{7465} = 1.6$ and $r_{7465} = 0.1$, respectively, and spectral classification in the two cases is done without consideration of veiling. In Case 3, the spectra are assumed to be taken at $r_{7465} = 0.1$, and the photometry at $r_{7465} = 1.6$; the converse is true for Case 4. For Cases 3 and 4, the open (circle or square) symbols are for spectral classification without considering veiling, and the filled (circle or square) symbols for classification that includes veiling.

7.3. Star Formation History in the NAP Complex

In Section 6.2, we have discussed the probable age differences among the kinematic groups within the NAP region, suggesting that there has been a multiple-epoch star formation process across the complex. Here, we investigate this issue from a different view using the number ratios between Class II and Class I type SEDs, designated henceforth as C II/C I.

We use the YSO catalog from Rebull et al. (2011) and in total find 596 Class II sources and 270 Class I sources in the field. We grid the NAP region spatially and calculate the C II/C I ratio at each grid point using the nearest 10 YSOs, including both Class II and Class I sources. In order to avoid noise from grid points where there are few or no identified YSOs, we set a threshold of 0.1 arcmin^{-2} on the YSO surface density centered at each grid point. The C II/C I ratios of the grid points with the minimum YSO surface density are used in Figure 26 to illustrate the variation of C II/C I over the NAP field.

Overall, the C II/C I ratio varies, and we can consider how the ratio changes among the identified kinematic groups. Within Group E, Class I sources are dominant (low C II/C I), while within Group F, the number of Class II is far greater than that of Class I sources (high C II/C I). Within Group D, two distinct regions can be noted. Near the center of this large group, the region is dominated by Class II sources (high C II/C I), and surrounding that area are several regions, including Group C, with C II/C I ≈ 1. Within Groups A and B, the surface densities of Class II and Class I sources are both below the threshold (0.1 arcmin^{-2}), but we note that their C II/C I are high at 7 and 3, respectively. Surrounding each of Group A and B are regions with relatively dense concentrations of Class II and Class I sources with C II/C I ratios ≈ 1. This is the same structure as noted above for Group D.

The C II/C I ratio has been explored as a tracer of the regional evolution of star formation (Gutermuth et al. 2011). An investigation of the correlation between the gas surface density and the YSO mass surface density with different C II/C I suggests that regions at early evolutionary stages tend to have low C II/C I and high gas surface density (Pokhrel et al. 2020). In the NAP, we also see the same trend that regions with low C II/C I are associated with dense gas material traced by the Planck 857 μm dust emission (see Figure 26). The strong variations in C II/C I over the NAP field demonstrated in Figure 26 suggest that star formation is not coeval across the cloud.

We further investigate the region centered on Group D using the YSOs that we have confirmed here with spectroscopy. According to their isochrone ages derived from the H-R diagram (see Figure 18), we can divide these YSOs having $T_{\rm eff} \geqslant 3000$ K into two categories: "young" YSOs with isochrone ages younger than 0.5 Myr and "old" YSOs with isochrone ages between 1 and 10 Myr. In Figure 27, we show the distributions of these two types of YSOs.

The majority of YSOs are distributed within the infrared bubble that is prominent in the WISE W3–band image. Intriguingly, while the "old" YSOs share the uniform distribution of the overall population, the "young" YSOs tend to be distributed near the boundary of the bubble, especially in the two dense molecular cores on the east and the west (Group C). This suggests that there has been sequential star formation within Group D—consistent with the result presented above from the study of the C II/C I ratio.

In combination with other results from the H-R diagram (see Section 6.2), our interpretation is that star formation has progressed from the region of Group F to Group D, then propagated to the regions surrounding Group D, including Group C, with Group E currently the most active site of star formation within the NAP region. Groups A and B do not have enough stars for age assessment, but seem consistent with the median age. We note that Bally et al. (2014) have discussed the most recent star formation history in the NAP region, as traced by outflows.

8. Summary

We have presented the first large-scale spectroscopic study of members and prospective members of the NAP region. The primary data set consists of $R \approx 1300$–2000 optical spectra of $\approx$3400 stars, which we combine with multiwavelength photometric data in order to create SEDs spanning $\sim$0.4–25 μm. We also consider the photometric variability of the spectroscopic sample using ZTF data.

We first assess the membership of each source in the spectroscopic sample by considering the evidence for Li I absorption in the spectra, X-ray emission from cross-referencing to published data, and infrared excess emission from the spectral slopes we derive based on published photometry or new photometric analysis that we have conducted for stars without previously published measurements. We further assess the membership of these subsamples using Gaia astrometry. Considering only likely members, we then use the spectra and the broadband SEDs to derive stellar parameters. These include spectral type and photospheric temperature, continuum veiling, foreground extinction, and bolometric luminosity.

Beyond presenting our catalog of $\approx$600 confirmed members and their stellar parameters, our scientific results include the following:

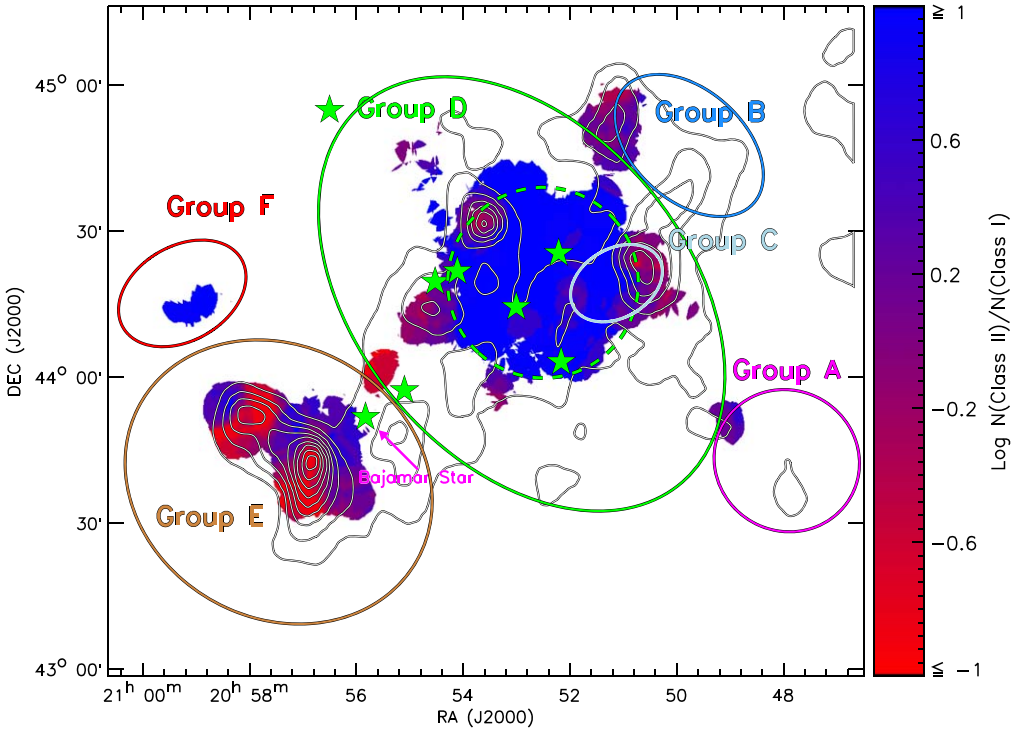

Figure 26. Number ratio between Class II and Class I sources in the NAP, shown in a color scale. The color bar is shown. The green filled star symbols show the O- or B-type stars. The contours show the Planck 857 μm dust emission.

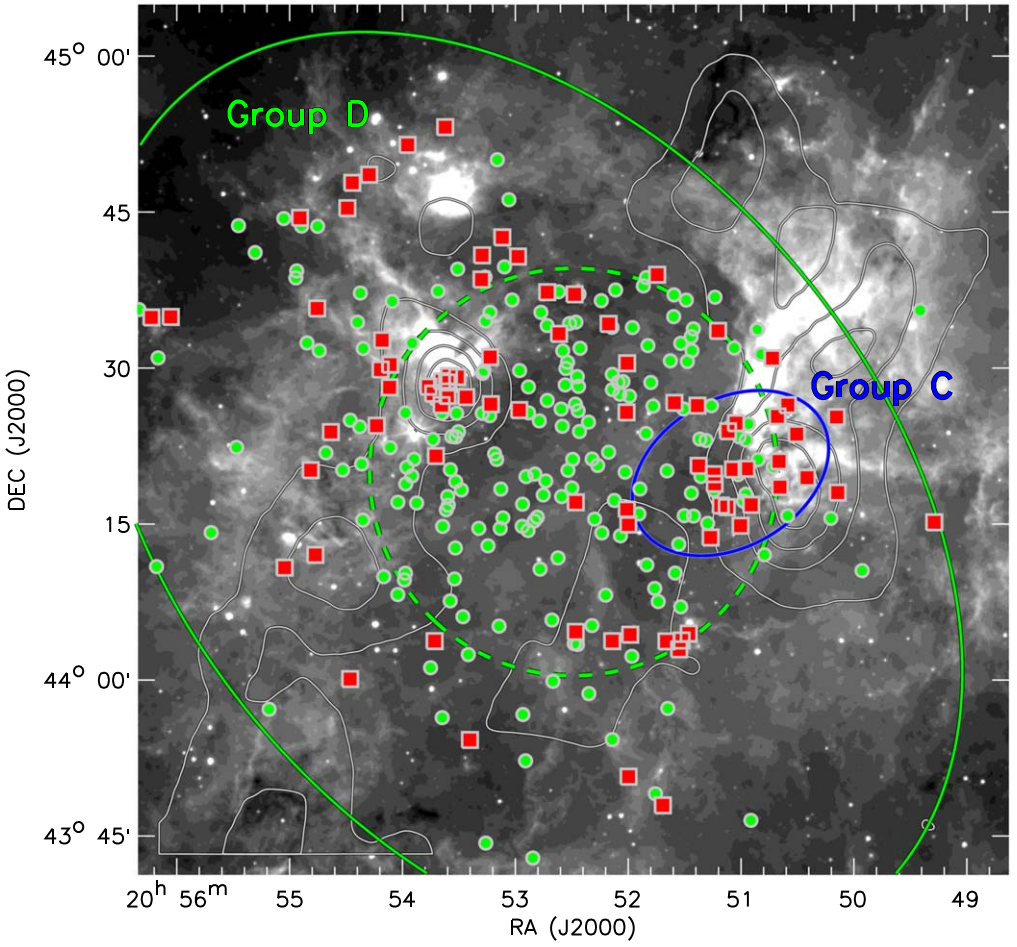

Figure 27. Distribution of YSOs centered at Group D overplotted on the image in the WISE W3 band. The red filled squares are for the YSOs with isochrone ages younger than 0.5 Myr, and the green filled circles are for those with isochrone ages between 1 and 10 Myr. The contours show the Planck 857 μm dust emission. The green dashed circle is the same as in Figure 26.

1. The H-R diagram for our spectroscopic sample spans masses from a $\sim$6 $M_{\odot}$ B7 star to several 0.09 $M_{\odot}$ M7 stars. We note that the region contains two more massive O-type stars that are not part of our spectroscopic survey.
2. The median age of the sample is 1 Myr and the luminosity dispersion is $\sim$0.3–0.4 dex. The observed photometric variability does not significantly contribute to the luminosity dispersion.
3. Incompleteness at the low-mass end precludes us from making any conclusions about the mass distribution.
4. Different kinematic subgroups appear to have different ages. The star formation history in the region began with Group F, continued in Group D, and extended to the regions surrounding Group D, including Group C, with Group E currently the most active site of star formation.

We also highlight and extensively discuss the systematic effects of veiling on stellar spectral typing and quantify the errors that are made when veiling is not accounted for. One specific object with substantial veiling variability measured among our several spectra is used to demonstrate the significant impact of veiling.

Many thanks to the anonymous referee for comments that helped to improve this paper. We thank Michael A. Kuhn for discussions about the NAP region. We recognize the contributions of former Caltech SURF students Daniel DeFelippis and Danika Wellington to our efforts. This paper uses data products produced by the OIR Telescope Data Center, supported by the Smithsonian Astrophysical Observatory. This work has made use of data from the European Space Agency mission Gaia (https://www.cosmos.esa.int/gaia), processed by the Gaia Data Processing and Analysis Consortium (DPAC; https://www.cosmos.esa.int/web/gaia/dpac/consortium). Funding for the DPAC has been provided by national institutions, in particular the institutions participating in the Gaia Multilateral Agreement. We use ZTF data, enabled by support from the National Science Foundation under grant AST-1440341, Caltech, IPAC, the Weizmann Institute for Science, the Oskar Klein Centre at Stockholm University, the University of Maryland, the University of Washington, Deutsches Elektronen-Synchrotron and Humboldt University, Los Alamos National Laboratories, the TANGO Consortium of Taiwan, the University of Wisconsin at Milwaukee, and Lawrence Berkeley National Laboratories.

Facilities: Palomar:P200 (Norris), Keck:I (DEIMOS), MMT (Hectospec), Palomar:P48 (ZTF).

Appendix A
Improvement in IRAC Photometry

In this work, we prefer to use the Spitzer photometry for our sources (mostly with infrared excess emission) collected from Rebull et al. (2011). For those without photometry in Rebull et al. (2011), we collect the aperture photometry in the 3.″8 aperture from SEIP. However, we notice some photometry from SEIP is unreliable, which could be due to the strong and highly variable background in the field, and some field stars could be misclassified as having infrared excess emission (see Figure 28). For those sources, we use our point-spread function photometry, which is performed as described in Fang et al. (2009). A comparison of the photometry for four sources from SEIP and ours is shown in Figure 28.

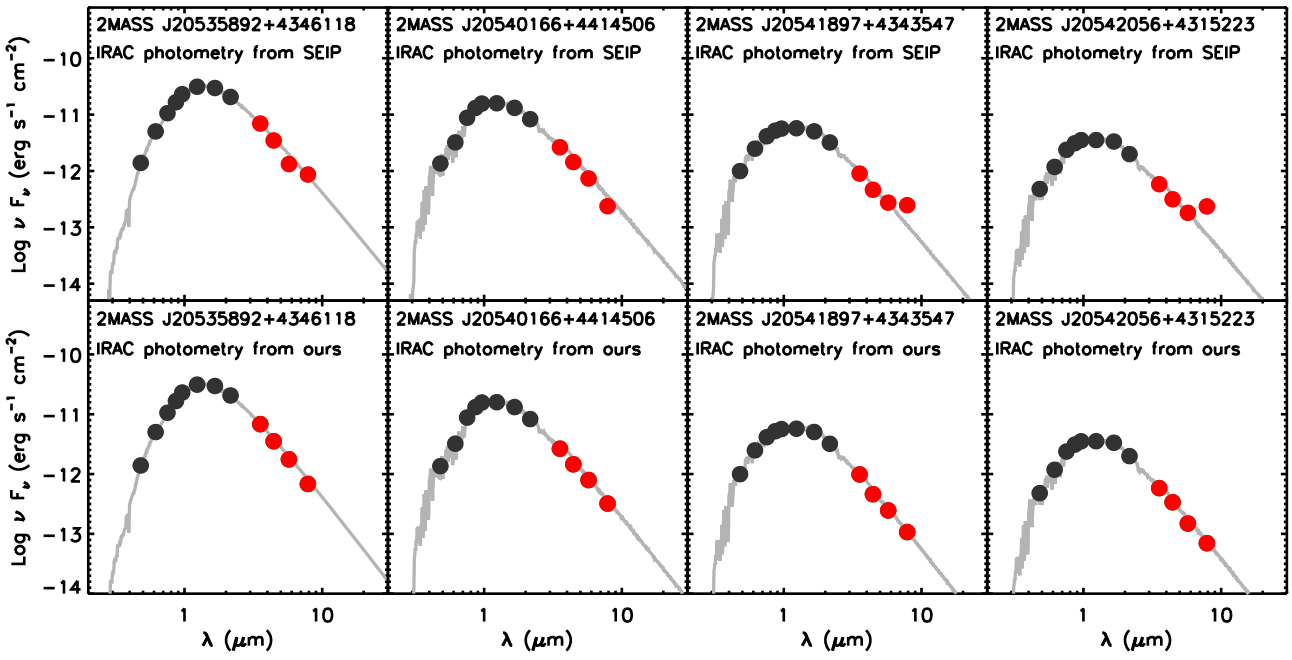

Figure 28. SEDs of four sources with bad IRAC photometry in at least one band from SEIP (top panels) and the IRAC photometry from this work (bottom panels). In each panel, the black filled circles are the photometry from Pan-STARRS and 2MASS, and the red filled circles are the photometry in the Spitzer IRAC bands. The gray line is the photospheric level.

Table 6
List of Nonmembers of NAP with Infrared Excess in Our Sample

ID	Name Designation	R.A. (J2000)	Decl. (J2000)	Gaia Parallax (mas)	Spectral Type
1	2MASS J20491197+4414123	20 49 11.98	+44 14 12.3	0.3323 ± 0.0448	F8.0
2	2MASS J20492960+4400467	20 49 29.60	+44 00 46.7	−0.1801 ± 0.0866	Late B
3	2MASS J20510271+4349318	20 51 02.71	+43 49 31.9	0.4564 ± 0.0269	Early B
4	2MASS J20511071+4306142	20 51 10.72	+43 06 14.2	0.3829 ± 0.0694	Late B
5	2MASS J20511500+4409006	20 51 15.01	+44 09 00.7	0.5238 ± 0.0236	A8.8
6	2MASS J20512307+4426461	20 51 23.08	+44 26 46.2	0.3227 ± 0.0841	B7.4
7	2MASS J20513007+4412312	20 51 30.07	+44 12 31.3	0.2102 ± 0.1775	A7.6
8	2MASS J20513811+4415493	20 51 38.12	+44 15 49.3	0.2225 ± 0.2150	A9.7
9	2MASS J20514755+4425106	20 51 47.55	+44 25 10.6	0.3214 ± 0.0370	A8.6
10	2MASS J20523733+4305467	20 52 37.33	+43 05 46.8	0.3788 ± 0.0174	Early B
11	2MASS J20525419+4321189	20 52 54.20	+43 21 18.9	1.0723 ± 0.0277	A7.7
12	2MASS J20533175+4501286	20 53 31.76	+45 01 28.6	0.1299 ± 0.0800	F1.9
13	2MASS J20533271+4449117	20 53 32.72	+44 49 11.8	0.1521 ± 0.0559	A9.9
14	2MASS J20533370+4447091	20 53 33.70	+44 47 09.2	−0.3471 ± 0.2115	A4.9
15	2MASS J20535583+4314147	20 53 55.83	+43 14 14.8	0.2336 ± 0.0313	A8.8
16	2MASS J20535754+4356476	20 53 57.55	+43 56 47.6	0.7018 ± 0.1191	F7.3
17	2MASS J20544690+4448197	20 54 46.90	+44 48 19.8	0.0564 ± 0.0876	Late B
18	2MASS J20545128+4306226	20 54 51.28	+43 06 22.6	0.3560 ± 0.0598	Late B–early A
19	2MASS J20552589+4446471	20 55 25.90	+44 46 47.1	0.2746 ± 0.1644	F1.9
20	2MASS J20553187+4447004	20 55 31.88	+44 47 00.5	0.2275 ± 0.0859	Early F
21	2MASS J20553791+4455205	20 55 37.91	+44 55 20.6	−0.4208 ± 0.3217	F7.4
22	2MASS J20553880+4456560	20 55 38.81	+44 56 56.1	−0.1639 ± 0.1716	F0.1
23	2MASS J20561239+4414182	20 56 12.39	+44 14 18.3	0.0812 ± 0.1894	A7.8
24	2MASS J20562155+4445145	20 56 21.56	+44 45 14.5	0.2396 ± 0.0950	A9.2
25	2MASS J20562449+4456225	20 56 24.50	+44 56 22.5	0.3407 ± 0.0631	Early B
26	2MASS J20564398+4404138	20 56 43.99	+44 04 13.9	...	O9.0
27	2MASS J20564699+4443555	20 56 46.99	+44 43 55.6	...	F1.8
28	2MASS J20564785+4438373	20 56 47.85	+44 38 37.3	0.2440 ± 0.0462	B8.0
29	2MASS J20573452+4359547	20 57 34.53	+43 59 54.7	1.0597 ± 0.0335	A7.8
30	2MASS J20574034+4410465	20 57 40.35	+44 10 46.6	−0.7086 ± 0.6578	Late B–early A
31	2MASS J20581722+4344091	20 58 17.23	+43 44 09.1	0.2349 ± 0.0812	A8.5
32	2MASS J20593917+4353527	20 59 39.17	+43 53 52.8	0.5561 ± 0.0266	B7.7
33	2MASS J20595153+4343302	20 59 51.53	+43 43 30.3	0.6124 ± 0.0435	F4.2
34	2MASS J20591724+4417464	20 59 17.25	+44 17 46.5	0.4070 ± 0.0232	Early B
35	2MASS J20532479+4351527	20 53 24.80	+43 51 52.7	0.0361 ± 0.0941	A7.3
36	2MASS J20485426+4356172	20 48 54.27	+43 56 17.3	0.3855 ± 0.1053	A9.2
37	2MASS J20545135+4515063	20 54 51.36	+45 15 06.3	0.1201 ± 0.0209	Early B
38	2MASS J20553631+4517182	20 55 36.32	+45 17 18.3	0.2048 ± 0.0348	B8.0
39	2MASS J20544203+4516532	20 54 42.03	+45 16 53.2	0.3647 ± 0.2272	B8.0
40	2MASS J21000826+4315030	21 00 08.27	+43 15 03.1	0.2417 ± 0.0593	F1.9

(This table is available in machine-readable form.)

Appendix B
Nonmembers with Infrared Excess

In our sample, 40 sources with infrared excess emission and spectral types earlier than G are excluded as nonmembers of the NAP, according to their locations in the H-R diagram and/or the Gaia parallax. These sources are listed in Table 6, which includes their Gaia parallax and spectral types.

Appendix C
A VY Scl Star

Among the sources identified with X-ray emission, we note one interesting object, LkHα 170 = HBC 297. This star is B8.5 according to our classification and A0 in Hernández et al. (2004). It is also an emission line star and thus a potential Herbig Ae/Be object. Given its parallax (1.2912 ± 0.0224), the star should be a member of the NAP. However, in the H-R diagram it appears about one order of magnitude fainter than main-sequence stars with the same spectral type. The source is also referred to in the literature in the context of VY Scl stars (Patterson et al. 2001). It is thus beyond the scope of this work.

ORCID iDs

Min Fang https://orcid.org/0000-0001-8060-1321
Jinyoung Serena Kim https://orcid.org/0000-0001-6072-9344
Krzysztof Findeisen https://orcid.org/0000-0003-1898-5760
Gregory J. Herczeg https://orcid.org/0000-0002-7154-6065
John M. Carpenter https://orcid.org/0000-0003-2251-0602
Luisa M. Rebull https://orcid.org/0000-0001-6381-515X
Hongchi Wang https://orcid.org/0000-0003-0746-7968

References

Allard, F., Homeier, D., & Freytag, B. 2011, in ASP Conf. Ser. 448, XVI Cambridge Workshop on Cool Stars, Stellar Systems, and the Sun, ed. C. Johns-Krull, M. K. Browning, & A. A. West (San Francisco, CA: ASP), 91

Asplund, M., Grevesse, N., Sauval, A. J., & Scott, P. 2009, ARA&A, 47, 481
Bally, J., Ginsburg, A., Probst, R., et al. 2014, AJ, 148, 120
Bally, J., & Scoville, N. Z. 1980, ApJ, 239, 121
Barden, S. C., & Armandroff, T. 1995, Proc. SPIE, 2476, 56
Bhardwaj, A., Panwar, N., Herczeg, G. J., Chen, W. P., & Singh, H. P. 2019, A&A, 627, A135
Cardelli, J. A., Clayton, G. C., & Mathis, J. S. 1989, ApJ, 345, 245
Chambers, K. C., Magnier, E. A., Metcalfe, N., et al. 2016, arXiv:1612.05560
Cohen, M., & Kuhi, L. V. 1979, ApJS, 41, 743
Comerón, F., & Pasquali, A. 2005, A&A, 430, 541
Cooper, M. C., Newman, J. A., Davis, M., Finkbeiner, D. P., & Gerke, B. F. 2012, spec2d: DEEP2 DEIMOS Spectral Pipeline, Astrophysics Source Code Library, ascl:1203.003
Damiani, F., Pillitteri, I., & Prisinzano, L. 2017, A&A, 602, A115
Faber, S. M., Phillips, A. C., Kibrick, R. I., et al. 2003, Proc. SPIE, 4841, 1657
Fabricant, D., Fata, R., Roll, J., et al. 2005, PASP, 117, 1411
Fang, M., Kim, J. S., Pascucci, I., et al. 2017, AJ, 153, 188
Fang, M., Kim, J. S., Pascucci, I., et al. 2020, ApJS, submitted
Fang, M., Kim, J. S., van Boekel, R., et al. 2013, ApJS, 207, 5
Fang, M., van Boekel, R., Wang, W., et al. 2009, A&A, 504, 461, (Paper I)
Feiden, G. A. 2016, A&A, 593, A99
Findeisen, K., Hillenbrand, L., Ofek, E., et al. 2013, ApJ, 768, 93
Fischer, W., Edwards, S., Hillenbrand, L., & Kwan, J. 2011, ApJ, 730, 73
Gaia Collaboration, Brown, A. G. A., Vallenari, A., et al. 2018, A&A, 616, A1
Gaia Collaboration, Prusti, T., de Bruijne, J. H. J., et al. 2016, A&A, 595, A1
Garmany, C. D., Conti, P. S., & Chiosi, C. 1982, ApJ, 263, 777
Goy, G. 1973, A&AS, 12, 277
Greiner, J., Tovmassian, G. H., Di Stefano, R., et al. 1999, A&A, 343, 183
Guieu, S., Rebull, L. M., Stauffer, J. R., et al. 2009, ApJ, 697, 787
Gutermuth, R. A., Pipher, J. L., Megeath, S. T., et al. 2011, ApJ, 739, 84
Hamilton, D., Oke, J. B., Carr, M. A., et al. 1993, PASP, 105, 1308
Herbig, G. H. 1958, ApJ, 128, 259
Herczeg, G. J., & Hillenbrand, L. A. 2014, ApJ, 786, 97
Hernández, J., Calvet, N., Briceño, C., Hartmann, L., & Berlind, P. 2004, AJ, 127, 1682
Hillenbrand, L. A., Bauermeister, A., & White, R. J. 2008, in ASP Conf. Ser. 384, XIV Cambridge Workshop on Cool Stars, Stellar Systems, and the Sun, ed. G. van Belle (San Francisco, CA: ASP), 200
Husser, T. O., Wende-von Berg, S., Dreizler, S., et al. 2013, A&A, 553, A6
Kuhn, M. A., Hillenbrand, L. A., Carpenter, J. M., & Avelar Menendez, A. R. 2020, ApJ, 899, 128
Lynds, B. T. 1962, ApJS, 7, 1
Maíz Apellániz, J., Alonso Moragón, A., Ortiz de Zárate Alcarazo, L. & GOSSS Team 2017, in Highlights on Spanish Astrophysics IX, ed. S. Arribas et al. (Bilbao, Spain), 509
Manara, C. F., Frasca, A., Alcalá, J. M., et al. 2017, A&A, 605, A86
Manara, C. F., Testi, L., Rigliaco, E., et al. 2013, A&A, 551, A107
Masci, F. J., Laher, R. R., Rusholme, B., et al. 2019, PASP, 131, 018003
Matthews, H. E., & Goss, W. M. 1980, A&A, 88, 267
Mészáros, S., Allende Prieto, C., Edvardsson, B., et al. 2012, AJ, 144, 120
Miller, A. A., Hillenbrand, L. A., Covey, K. R., et al. 2011, ApJ, 730, 80
Mink, D. J., Wyatt, W. F., Caldwell, N., et al. 2007, in ASP Conf. Ser. 376, Astronomical Data Analysis Software and Systems XVI, ed. R. A. Shaw, F. Hill, & D. J. Bell (San Francisco, CA: ASP), 249
Morgan, W. W., Strömgren, B., & Johnson, H. M. 1955, ApJ, 121, 611
Muench, A. A., Lada, E. A., Lada, C. J., & Alves, J. 2002, ApJ, 573, 366
Newman, J. A., Cooper, M. C., Davis, M., et al. 2013, ApJS, 208, 5
O'Dell, C. R., Kollatschny, W., & Ferland, G. J. 2017, ApJ, 837, 151
Patterson, J., Thorstensen, J. R., Fried, R., et al. 2001, PASP, 113, 72
Pokhrel, R., Gutermuth, R. A., Betti, S. K., et al. 2020, ApJ, 896, 60
Rebull, L. M., Guieu, S., Stauffer, J. R., et al. 2011, ApJS, 193, 25
Reipurth, B., & Schneider, N. 2008, in Star Formation and Young Clusters in Cygnus, Vol. 4, ed. B. Reipurth (San Francisco, CA: ASP), 36
Rugel, M., Fedele, D., & Herczeg, G. 2018, A&A, 609, A70
Semkov, E. H., Peneva, S. P., Munari, U., Milani, A., & Valisa, P. 2010, A&A, 523, L3
Skrutskie, M. F., Cutri, R. M., Stiening, R., et al. 2006, AJ, 131, 1163
Teplitz, H. I., Capak, P., Hanish, D., et al. 2012, AAS Meeting 219, 428.06
Welin, G. 1973, A&AS, 9, 183
Wendker, H. J., Benz, D., & Baars, J. W. M. 1983, A&A, 124, 116
Zhang, S., Xu, Y., & Yang, J. 2014, AJ, 147, 46